

Integration of adversarial autoencoders with residual dense convolutional networks for estimation of non-Gaussian hydraulic conductivities

Shaoxing Mo^{1,2}, Nicholas Zabar², Xiaoqing Shi¹, and Jichun Wu¹

¹Key Laboratory of Surficial Geochemistry of Ministry of Education, School of Earth Sciences and Engineering, Nanjing University, Nanjing, China.

²Center for Informatics and Computational Science, University of Notre Dame, Notre Dame, IN, USA.

Key Points:

- A convolutional adversarial autoencoder is developed to parameterize non-Gaussian conductivity fields with multimodal distributions
- A deep residual dense convolutional network is introduced as a surrogate of the forward physics-based model
- The integrated method is tested with inverse problems for the estimation of non-Gaussian conductivities in solute transport modeling

arXiv:1906.11828v4 [physics.comp-ph] 13 Jan 2020

Corresponding author: Nicholas Zabar, nzabar@gmail.com

Corresponding author: Xiaoqing Shi, shixq@nju.edu.cn

Abstract

Inverse modeling for the estimation of non-Gaussian hydraulic conductivity fields in subsurface flow and solute transport models remains a challenging problem. This is mainly due to the non-Gaussian property, the non-linear physics, and the fact that many repeated evaluations of the forward model are often required. In this study, we develop a convolutional adversarial autoencoder (CAAE) to parameterize non-Gaussian conductivity fields with heterogeneous conductivity within each facies using a low-dimensional latent representation. In addition, a deep residual dense convolutional network (DRDCN) is proposed for surrogate modeling of forward models with high-dimensional and highly-complex mappings. The two networks are both based on a multilevel residual learning architecture called residual-in-residual dense block. The multilevel residual learning strategy and the dense connection structure ease the training of deep networks, enabling us to efficiently build deeper networks that have an essentially increased capacity for approximating mappings of very high-complexity. The CCAE and DRDCN networks are incorporated into an iterative ensemble smoother to formulate an inversion framework. The numerical experiments performed using 2-D and 3-D solute transport models illustrate the performance of the integrated method. The obtained results indicate that the CCAE is a robust parameterization method for non-Gaussian conductivity fields with different heterogeneity patterns. The DRDCN is able to obtain accurate approximations of the forward models with high-dimensional and highly-complex mappings using relatively limited training data. The CCAE and DRDCN methods together significantly reduce the computation time required to achieve accurate inversion results.

1 Introduction

Groundwater flow and solute transport models are used widely to help understand subsurface processes and make science-informed decisions for groundwater resource management. Reliable model predictions that well reproduce the phenomena of interest require a good characterization of the hydraulic conductivity field as it greatly influences groundwater flow and solute transport. In many practical cases, such as aquifers in fluvial deposits where several highly contrasting facies coexist, it may be unrealistic to model the log-conductivity as a multivariate Gaussian. It has been shown that a multimodal distribution can better characterize the connectivity between different facies and the multimodality in highly heterogeneous conductivity fields (Gómez-Hernández & Wen, 1998; Journel & Deutsch, 1993; Kerrou et al., 2008; Zhou et al., 2014).

In this study, we are concerned with an inverse estimation of non-Gaussian conductivity fields with heterogeneous conductivity within each facies using hydraulic head and solute concentration data. This is in contrast to categorical fields with homogeneous conductivity within each facies (e.g., the binary field) (Winter et al., 2003), although they both have multimodal distributions. In practice, the conductivity field is estimated via inverse modeling. Commonly used inverse methods are, for example, Markov chain Monte Carlo methods (Vrugt, 2016) and the ensemble-based data assimilation methods such as ensemble smoother (van Leeuwen & Evensen, 1996), ensemble Kalman filter (Evensen, 1994), and their variants (Emerick & Reynolds, 2013; Laloy et al., 2013; Sun et al., 2009; Xu & Gómez-Hernández, 2018; J. Zhang et al., 2018; Zhou et al., 2011). Considering the strong conductivity heterogeneity, the inverse problem is usually high-dimensional. Thus, it often requires a large number of forward model runs to obtain converged inversion results.

To relieve the large computational cost, parameterization methods are commonly used together with surrogate models within the inversion framework. A parameterization method aims to represent the spatially correlated property field using a low-dimensional latent vector (Linde et al., 2015; Oliver & Chen, 2011; Zhou et al., 2014). It can also 1) mitigate the potential ill-posedness of the inverse problem, 2) ensure that the updated fields in the inversion process satisfy the prior distribution assumptions (e.g., non-Gaussian) imposed on

the unknown field, and 3) produce normally distributed latent variables, allowing direct use of second-order inverse methods (e.g., ensemble smoother and ensemble Kalman filter), although these may be at the cost of increased nonlinearity for the inverse problems (Laloy et al., 2019). In previous studies involving the estimation of non-Gaussian conductivity fields, as noted in the review by Linde et al. (2015), one popular solution is to utilize multiple-point statistics (MPS) simulation in the inversion to generate conductivity field realizations that honor the non-Gaussian prior determined by a training image (Hansen et al., 2012; Laloy et al., 2016; Mariethoz et al., 2010; Zahner et al., 2016). While such MPS-based inverse methods can generally provide reliable estimations, they may be computationally intensive (Laloy et al., 2018). A surrogate method aims to replace the computationally expensive forward model with an accurate but cheap-to-run surrogate model during the inversion (Asher et al., 2015; Razavi et al., 2012). Although such combinations of methods for inverse modeling have been intensively studied for problems with Gaussian conductivity fields (Chang et al., 2017; Elsheikh et al., 2014; Ju et al., 2018; Laloy et al., 2013; J. Zhang et al., 2015, 2016), previous studies on problems with non-Gaussian conductivity fields often relied on the inverse methods solely without using the parameterization and surrogate methods. The development of parameterization and surrogate methods for such non-Gaussian problems remains an open problem due to two major challenges.

First, most existing parameterization methods fail to work for non-Gaussian conductivity fields. Previous works on parameterizing the conductivity fields in inversion has relied on, for example, principal component analysis and its variants (Ma & Zabaras, 2011; Sarma et al., 2008; Vo & Durlinsky, 2014; D. Zhang & Lu, 2004). While these methods are well suited for Gaussian random fields, their performance for complex non-Gaussian fields deserves further improvement (Canchumuni et al., 2019b; Chan & Elsheikh, 2017; Laloy et al., 2017; Y. Liu et al., 2019). Inspired by the recent success of deep learning in various areas including Earth science (Bergen et al., 2019; Reichstein et al., 2019; Zuo et al., 2019) and hydrology (Shen, 2018), its application in parameterization of non-Gaussian conductivity fields has been reported in many recent studies (Canchumuni et al., 2019a, 2019b; Chan & Elsheikh, 2017, 2018, 2019; Laloy et al., 2017, 2018; Y. Liu et al., 2019). Among these applications, generative adversarial network (GAN) (Goodfellow et al., 2014) and variational autoencoder (VAE) (Kingma & Welling, 2014) are the two most popular network architectures. After training the network, these methods take random realizations of a low-dimensional vector as input and then generate new realizations of the conductivity field having similar features with those found in the training data. The quality of the generated realizations was shown to be superior to those from traditional parameterization methods (Canchumuni et al., 2019b; Chan & Elsheikh, 2017; Laloy et al., 2017; Y. Liu et al., 2019). However, these methods focused on categorical conductivity fields with homogeneous conductivity within each facies. Their applicability to non-Gaussian fields with heterogeneous conductivity within each facies, which is more challenging, remains to be further investigated. Laloy et al. (2018) and Y. Liu et al. (2019) further tested their methods' potential for such continuous fields. While the results suggested a promising performance of the deep learning-based parameterization methods, no inversion results were presented. Canchumuni et al. (2019b) considered channelized conductivity fields with a bimodal distribution. They used a VAE network to generate binary channelized fields and the uncertain parameters to be estimated in the inversion are the latent variables and the permeability values at all grid points, with the inverse problem remaining high-dimensional.

Second, most existing surrogate methods suffer from the curse of dimensionality (Asher et al., 2015; Razavi et al., 2012) and fail to efficiently obtain accurate approximations when the input-output relations are highly-nonlinear (Liao et al., 2017; Lin & Tartakovsky, 2009; Mo et al., 2017). The curse of dimensionality is caused by the exponentially increased computational cost required for accurate surrogate construction as the input dimensionality (i.e., the number of uncertain variables considered) increases. Due to the strongly heterogeneous nature of the conductivity field, it is often required to use a large number of stochastic degrees of freedom to accurately represent the heterogeneity. The highly-nonlinear outputs

here arise because the high-conductivity regions in a non-Gaussian aquifer result in preferential paths for the groundwater flow and solute transport. The two factors together make the commonly used surrogate methods, such as Gaussian processes (Rasmussen & Williams, 2006) and polynomial chaos expansion (Xiu & Karniadakis, 2002), difficult to work. Deep neural networks have already exhibited a promising and impressive performance for surrogate modeling of forward models with high-dimensional input and output fields (Kani & Elsheikh, 2019; Mo, Zabararas, et al., 2019; Mo, Zhu, et al., 2019; Sun, 2018; Tripathy & Billionis, 2018; Zhong et al., 2019; Zhu & Zabararas, 2018; Zhu et al., 2019). For example, in Tripathy and Billionis (2018) a deep neural network was proposed to build a surrogate model for a single-phase flow forward model. In Sun (2018) and Zhong et al. (2019), their surrogate methods for a single-phase flow forward model and a multiphase flow forward model, respectively, were based on an adversarial network framework. In our previous studies (Mo, Zabararas, et al., 2019; Mo, Zhu, et al., 2019; Zhu & Zabararas, 2018; Zhu et al., 2019), a deep dense convolutional network (DDCN), which is based on a dense connection structure (Huang et al., 2017) for better information flow efficiency, was employed as the surrogate modeling framework. It showed a good performance in efficiently obtaining accurate surrogates of various forward models with high-dimensional input-output mappings. However, these methods were tested on forward models with Gaussian conductivity fields (Kani & Elsheikh, 2019; Mo, Zabararas, et al., 2019; Mo, Zhu, et al., 2019; Tripathy & Billionis, 2018; Zhu & Zabararas, 2018; Zhu et al., 2019) or on a single-phase flow model with binary channelized conductivity fields (Zhu et al., 2019). As shown in a case study below, the application of the DDCN surrogate method to solute transport modeling with non-Gaussian conductivity fields may lead to large approximation errors.

In this work, we develop a convolutional adversarial autoencoder (CAAE) to parameterize non-Gaussian conductivity fields with multimodal distributions. We transform a fully-connected adversarial autoencoder (Makhzani et al., 2016) to a convolutional network so as to improve its scalability for larger-size inputs. In addition, we propose a deep residual dense convolutional network (DRDCN) for efficient surrogate modeling of forward models with high-dimensional and highly-complex mappings. Although deeper networks have the potential to substantially improve the network’s performance, they can be difficult to train. We adopt in DRDCN a multilevel residual learning structure (X. Wang et al., 2018). The residual learning strategy has been shown to be an effective solution to ease the training of very deep networks (He et al., 2016a, 2016b; Simonyan & Zisserman, 2015; Szegedy et al., 2015; X. Wang et al., 2018). The multilevel residual learning structure is also implemented in the CAAE network. The CAAE and DRDCN networks are combined with an iterative local updating ensemble smoother (ILUES) algorithm (J. Zhang et al., 2018) to formulate an efficient CAAE-DRDCN-ILUES inversion framework. The overall integrated method is demonstrated using 2-D and 3-D solute transport modeling with non-Gaussian conductivity fields that have different heterogeneity patterns.

In summary, three major innovative contributions are addressed in this study. First, we develop a CAAE method for parameterization of non-Gaussian conductivity fields with heterogeneous conductivity within each facies that is suitable in the context of inverse modeling. Second, we adopt a multilevel residual strategy in our previous DDCN method (Mo, Zabararas, et al., 2019; Mo, Zhu, et al., 2019; Zhu & Zabararas, 2018; Zhu et al., 2019) to introduce a new DRDCN method with a substantially improved performance for surrogate modeling of highly-complex mappings. Finally and most importantly, to the best of our knowledge, we present the first attempt to incorporate simultaneously the parameterization and surrogate methods to perform inversion for non-Gaussian conductivities in solute transport modeling.

The rest of the paper is organized as follows. In section 2, we introduce a solute transport model and define the problem of interest. The CAAE-DRDCN-ILUES inversion framework is presented in section 3. Then in sections 4 and 5, the proposed method is evaluated using two synthetic examples. The conclusions are summarized in the last section.

2 Problem Definition

We consider solute transport in heterogeneous porous media under a steady-state groundwater flow condition. It is assumed that the transport of solute is driven by advection and dispersion. The governing equations for the steady-state flow and solute transport are written as (Zheng & Wang, 1999)

$$\nabla \cdot (K\nabla h) = 0, \quad (1)$$

and

$$\frac{\partial(\phi c)}{\partial t} = \nabla \cdot (\phi\boldsymbol{\alpha}\nabla c) - \nabla \cdot (\phi\mathbf{v}c) + r_s, \quad (2)$$

respectively. Here K (LT^{-1}) is the hydraulic conductivity, h (L) is the hydraulic head, ϕ (-) is the effective porosity, c (ML^{-3}) is the solute concentration, t (T) denotes time, r_s ($\text{ML}^{-3}\text{T}^{-1}$) is the sink/source, and $\boldsymbol{\alpha}$ (L^2T^{-1}) is the dispersion tensor determined by the pore space flow velocity \mathbf{v} (LT^{-1}), and longitudinal (α_L ; L), transverse (α_T ; L), and vertical (α_V ; L) dispersivities. The two equations are coupled through the velocity $\mathbf{v} = -\frac{K}{\phi}\nabla h$. The flow and solute transport equations are numerically solved using the MODFLOW (Harbaugh et al., 2000) and MT3DMS (Zheng & Wang, 1999) simulators, respectively.

We are concerned with an inverse problem of characterizing the heterogeneous conductivity field using measurements of the hydraulic head and concentration. The underlying conductivity fields of interest are non-Gaussian fields with a multimodal distribution. The inverse modeling is performed using the ILUES inversion algorithm (J. Zhang et al., 2018) which has shown a promising performance for high-dimensional and highly-nonlinear inverse problems (Mo, Zabararas, et al., 2019; J. Zhang et al., 2018).

3 Methodology

3.1 ILUES for Inverse Modeling

The ILUES algorithm assimilates the output measurements $\mathbf{d} \in \mathbb{R}^{N_d}$ for multiple times with an inflated covariance matrix of the measurement errors to avoid overweighing the measurements (J. Zhang et al., 2018). The inflated covariance matrix is often taken as $\tilde{\mathbf{C}}_D = N_{\text{iter}}\mathbf{C}_D$, where \mathbf{C}_D is the original covariance matrix of the measurement errors and N_{iter} is the number of iterations (Emerick & Reynolds, 2013; J. Zhang et al., 2018). To better handle high-dimensional and highly-nonlinear problems, ILUES also adopts a local updating scheme, which updates each input sample $\mathbf{m} \in \mathbb{R}^{N_m}$ (in the CAAE-DRDCN-ILUES framework, \mathbf{m} refers to the latent variables, see section 3.4) in the ensemble locally using its neighboring samples rather than all samples in the ensemble. Formally, given an ensemble of N_e input samples $\mathbf{M} = [\mathbf{m}_1, \dots, \mathbf{m}_{N_e}]$, it first identifies a local ensemble for each sample $\mathbf{m}_i \in \mathbf{M}$ based on the following metric (J. Zhang et al., 2018)

$$J(\mathbf{m}) = \frac{J_d(\mathbf{m})}{J_d^{\max}} + \frac{J_m(\mathbf{m})}{J_m^{\max}}, \quad (3)$$

where $J_d(\mathbf{m}) = [f(\mathbf{m}) - \mathbf{d}]^\top \mathbf{C}_D^{-1} [f(\mathbf{m}) - \mathbf{d}]$ quantifies the mismatch between the model responses $f(\mathbf{m})$ and measurements \mathbf{d} , and $J_m(\mathbf{m}) = (\mathbf{m} - \mathbf{m}_i)^\top \mathbf{C}_{\text{MM}}^{-1} (\mathbf{m} - \mathbf{m}_i)$ is the distance between the sample $\mathbf{m} \in \mathbf{M}$ and \mathbf{m}_i . Here, \mathbf{C}_{MM} is the autocovariance matrix of the input parameters in \mathbf{M} , J_d^{\max} and J_m^{\max} are the maximum values of $J_d(\cdot)$ and $J_m(\cdot)$, respectively. Based on the J values, we select $N_l = \beta_l N_e$, ($\beta_l \in (0, 1]$) samples as the local ensemble of \mathbf{m}_i using a roulette wheel selection operator (Lipowski & Lipowska, 2012), in which the selection probability of the i th individual is given as $P_i = \rho_i / \sum_{j=1}^{N_e} \rho_j$, $i = 1, \dots, N_e$, where $\rho_j = 1/J(\mathbf{m}_j)$ (Mo, Zabararas, et al., 2019). A local ensemble factor of $\beta_l = 0.1$ suggested in J. Zhang et al. (2018) is used.

Let superscripts l , f , and a denote the local ensemble, current and updated samples, respectively. The ILUES first updates the local ensemble of each sample $\mathbf{m}_i^f \in \mathbf{M}^f$, that is,

$\mathbf{M}_i^{l,f}$, by using the usual ensemble smoother scheme (Emerick & Reynolds, 2013; J. Zhang et al., 2018):

$$\mathbf{m}_{i,j}^a = \mathbf{m}_{i,j}^f + \mathbf{C}_{\text{MD}}^{l,f} (\mathbf{C}_{\text{DD}}^{l,f} + \tilde{\mathbf{C}}_{\text{D}})^{-1} [\mathbf{d}_j - f(\mathbf{m}_{i,j}^f)], \quad (4)$$

for $j = 1, \dots, N_l$. Here $\mathbf{C}_{\text{MD}}^{l,f}$ is the cross-covariance matrix between $\mathbf{M}_i^{l,f}$ and $\mathbf{D}_i^{l,f} = [f(\mathbf{m}_{i,1}^f), \dots, f(\mathbf{m}_{i,N_l}^f)]$, $\mathbf{C}_{\text{DD}}^{l,f}$ is the autocovariance matrix of $\mathbf{D}_i^{l,f}$, and $\mathbf{d}_j = \mathbf{d} + \tilde{\mathbf{C}}_{\text{D}}^{1/2} \mathbf{r}_{N_d}$, $\mathbf{r}_{N_d} \sim \mathcal{N}(\mathbf{0}, \mathbf{I})$, is the j -th realization of the measurements. The update of \mathbf{m}_i^f , \mathbf{m}_i^a , is then generated from its updated local ensemble $\mathbf{M}_i^{l,a} = [\mathbf{m}_{i,1}^a, \dots, \mathbf{m}_{i,N_l}^a]$ through a probabilistic scheme (Mo, Zabarar, et al., 2019). One update iteration of ILUES is summarized in Algorithm 1. More details regarding ILUES can be found in J. Zhang et al. (2018) and Mo, Zabarar, et al. (2019).

Algorithm 1 One update iteration in iterative local updating ensemble smoother. RWS: roulette wheel selection.

Require: Measurements \mathbf{d} , ensemble size N_e , local ensemble size factor β_l , current input ensemble $\mathbf{M}^f = [\mathbf{m}_1^f, \dots, \mathbf{m}_{N_e}^f]$ and output ensemble $\mathbf{D}^f = [f(\mathbf{m}_1^f), \dots, f(\mathbf{m}_{N_e}^f)]$.

- 1: $N_l \leftarrow \beta_l N_e$.
 - 2: **for** $i = 1, \dots, N_e$ **do** ▷ Update each sample using its local ensemble
 - 3: Given \mathbf{m}_i^f , compute the J values for samples in \mathbf{M}^f using equation (3).
 - 4: Choose the local ensemble of \mathbf{m}_i^f , $\mathbf{M}_i^{l,f} = [\mathbf{m}_{i,1}^f, \dots, \mathbf{m}_{i,N_l}^f]$, using RWS based on the J values.
 - 5: Obtain the updated local ensemble $\mathbf{M}_i^{l,a} = [\mathbf{m}_{i,1}^a, \dots, \mathbf{m}_{i,N_l}^a]$ using equation (4).
 - 6: Randomly draw a sample $\mathbf{m}_{i,j}^a \in \mathbf{M}_i^{l,a}$ and run the forward model $f(\mathbf{m}_{i,j}^a)$. ▷
 In CAAE-DRDCN-ILUES $f(\cdot)$ is computed using the surrogate model instead (see section 3.4)
 - 7: $r_a = \min\{1, \exp[-0.5(J_d(\mathbf{m}_{i,j}^a) - J_d(\mathbf{m}_i^f))]\}$. ▷ $J_d(\cdot)$ is defined in equation (3).
 - 8: $[\mathbf{m}_i^a, f(\mathbf{m}_i^a)] = \begin{cases} [\mathbf{m}_{i,j}^a, f(\mathbf{m}_{i,j}^a)], & \gamma \leq r_a \\ [\mathbf{m}_i^f, f(\mathbf{m}_i^f)], & \gamma > r_a \end{cases}$, where $\gamma \sim \mathcal{U}[0, 1]$.
 - 9: **end for**
 - 10: $\mathbf{M}^a = [\mathbf{m}_1^a, \dots, \mathbf{m}_{N_e}^a]$, $\mathbf{D}^a = [f(\mathbf{m}_1^a), \dots, f(\mathbf{m}_{N_e}^a)]$.
 - 11: **return** $\mathbf{M}^a, \mathbf{D}^a$ ▷ The updated input and output ensembles
-

For high-dimensional inverse problems, large ensemble size and iteration number are usually needed for ILUES to obtain converged and reliable inversion results, resulting in a large computational cost in forward model runs. To reduce the computational burden, we propose a CAAE network for parameterizing the high-dimensional conductivity field using a low-dimensional latent vector and a DRDCN network to build an accurate but fast-to-run substitution of the forward model in the ILUES algorithm.

3.2 DRDCN for Surrogate Modeling

In the surrogate modeling task, we build a surrogate model to approximate the mapping between the input conductivity field and the output hydraulic head and concentration fields. In our previous studies (Mo, Zabarar, et al., 2019; Mo, Zhu, et al., 2019; Zhu & Zabarar, 2018; Zhu et al., 2019), we transformed the surrogate modeling task for problems with high-dimensional input and output fields in a 2-D domain to an image-to-image regression problem by using a DDCN network. In this network, the input and output fields were treated as images. Denoting $H \times W$ as the spatial discretization resolution of the domain, $\mathbf{x} \in \mathbb{R}^{n_x \times H \times W}$ and $\mathbf{y} \in \mathbb{R}^{n_y \times H \times W}$ as the input and output fields, respectively. Then the surrogate modeling task for approximating the input-output mapping,

$$f : \mathbb{R}^{n_x \times H \times W} \rightarrow \mathbb{R}^{n_y \times H \times W}, \quad (5)$$

was transformed to an image regression problem between n_x input images and n_y output images with a resolution of $H \times W$, where n_x and n_y are the number of the input and output fields, respectively. It is straightforward to generalize to a 3-D domain by adding an extra depth axis to the images, that is, $\mathbb{R}^{n_x \times D \times H \times W} \rightarrow \mathbb{R}^{n_y \times D \times H \times W}$.

In order to further improve the performance of DDCN in problems with highly-complex mappings, we adopt a novel basic block called ‘residual-in-residual dense block’ proposed in X. Wang et al. (2018) for image super-resolution problems to formulate our DRDCN framework.

3.2.1 Residual-in-Residual Dense Block

A dense block introduces connections between non-adjacent layers aiming to fully exploit the hierarchical features from the outputs of preceding layers (Huang et al., 2017). Let $\mathbf{z}^{(i)}$ ($i = 1, \dots, L$) denote the output feature maps of the i th layer in the dense block, where L is number of layers. $\mathbf{z}^{(i)}$ is obtained by taking the concatenation of the output feature maps from its preceding layers as input, as represented by

$$\mathbf{z}^{(i)} = \mathcal{H}([\mathbf{z}^{(0)}, \dots, \mathbf{z}^{(i-1)}]), \quad (6)$$

where $\mathbf{z}^{(0)}$ represents the input to the dense block, and \mathcal{H} denotes operations on the input feature maps, including batch normalization (BN) (Ioffe & Szegedy, 2015), followed by nonlinear activation and convolution (Conv) (Goodfellow et al., 2016). The ReLU (Rectified Linear Unit) function defined as $\text{ReLU}(x) = \max(0, x)$ is commonly used. Alternatively, a new activation function Mish (Misra, 2019), which is defined as $\text{Mish}(x) = x \cdot \tanh(\ln(1 + e^x))$, can be used. It has been shown to perform generally better than ReLU in many deep networks across many datasets (Misra, 2019). A dense block with $L = 5$ layers is illustrated in Figure 1a.

It has been shown that deeper networks have the potential to better approximate mappings of high complexity, however, they can be difficult to train (Simonyan & Zisserman, 2015; Szegedy et al., 2015; X. Wang et al., 2018). To efficiently train a deeper network, we adopt a multilevel residual learning structure, that is, the residual-in-residual dense block proposed in X. Wang et al. (2018). In the residual learning framework, it has been shown that the residual mapping is much easier to learn than the original mapping (He et al., 2016a, 2016b). Specifically, let $f(\mathbf{x})$ denote the desired underlying mapping to fit. Then the stacked layers (not necessarily the entire network) learn the residual mapping $g(\mathbf{x}) := f(\mathbf{x}) - \mathbf{x}$. The original mapping $f(\mathbf{x})$ is then recast as $g(\mathbf{x}) + \mathbf{x}$. Such a residual learning strategy can help alleviate the gradient vanishing problem for deep network training (He et al., 2016a) and thus ease the training of very deep networks to achieve improved accuracy (He et al., 2016a, 2016b; Ledig et al., 2017; Simonyan & Zisserman, 2015; X. Wang et al., 2018).

The architecture of residual-in-residual dense block is shown in Figure 1b. It consists of a stack of residual dense blocks, where the residual learning is used in two levels, resulting in a residual-in-residual structure. That is, the residual learning implemented to the dense block results in a residual dense block; and that implemented to the stacked residual dense blocks results in a residual-in-residual dense block. The number of input and output feature maps of a dense block is N_f (Figure 1a) and is set to $N_f = 48$. In addition to the residual-in-residual structure, a residual scaling technique (Szegedy et al., 2016) is also employed in the residual-in-residual dense block to further increase the training stability (X. Wang et al., 2018). Formally, this is done by scaling down the residual $g(\mathbf{x})$ by a factor $\beta \in (0, 1]$ before adding to \mathbf{x} (Figure 1b). A factor of $\beta = 0.2$ suggested in X. Wang et al. (2018) is used in our network.

3.2.2 DRDCN Networks Based on Residual-in-Residual Dense Blocks

We employ the residual-in-residual dense block structure in our DRDCN network for surrogate modeling of solute transport in media with non-Gaussian conductivities. The

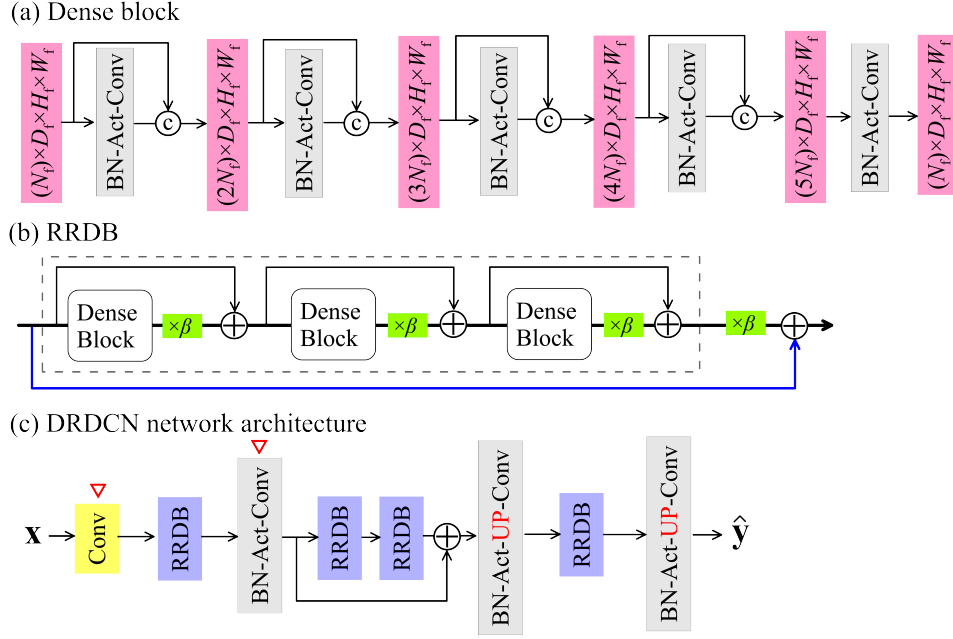


Figure 1: (a) A dense block with five layers. Each layer contains three operations (i.e., BN, Act, and Conv) and outputs N_f feature maps with size $D_f \times H_f \times W_f$, which are concatenated (\textcircled{C}) with its input feature maps. The concatenated feature maps are treated as the input to the next layer. (b) A residual-in-residual dense block (RRDB) with three residual dense blocks. The output of a dense block is scaled down by multiplying with a factor $\beta \in (0, 1]$ before adding (\oplus) to its input. (c) Architecture of the deep residual dense convolutional network (DRDCN). The feature map size is halved in Conv (∇) with stride 2 and doubled by using the nearest upsampling (UP) operation.

network architecture is shown in Figure 1c. For 2-D or 3-D images (fields), the 2-D and 3-D operations (i.e., BN and Conv) implemented in the PyTorch software are respectively used in the network. The network contains four residual-in-residual dense blocks and the feature maps are to go through a coarsen-to-refine process. A convolutional layer is first employed to extract feature maps from the raw input image. The obtained features are then passed through the residual-in-residual dense blocks and the transition convolutional layers for downsampling/upsampling of the feature maps. We arrange the position of the four residual-in-residual dense blocks in the network with a layout of (1, 2, 1) (Figure 1c) to encourage the information flow through the coarse feature maps. That is, one block is placed in the coarsening part; two adjacent blocks are placed in the most central part; and another one block is placed in the refining part. An additional level of residual learning is implemented to the stacked residual-in-residual dense blocks, resulting in a three-level residual learning structure in the network. In DRDCN, the Mish activation is used unless otherwise stated.

3.3 CAAE for Parameterization of Non-Gaussian Random Fields

We propose to parameterize non-Gaussian conductivity fields with multimodal distributions using a CAAE network. Without loss of generality, here we use \mathbf{x} to denote the log-conductivity field. Adversarial autoencoder is a probabilistic autoencoder that uses the GAN framework as a variational inference algorithm (Makhzani et al., 2016). The original adversarial autoencoder framework is composed of fully-connected layers (Makhzani et al., 2016), making it increasingly difficult to train as the network gets deeper due to a large num-

ber of trainable parameters. To resolve this issue, we develop a CAAE framework based on convolutional layers to leverage their sparse-connectivity and parameter-sharing properties as well as robust capability in image-like data processing (Goodfellow et al., 2016; Laloy et al., 2018; Mo, Zhu, et al., 2019; Shen, 2018).

3.3.1 Generative Adversarial Networks

GAN (Goodfellow et al., 2014) is a framework that establishes an adversarial game between two networks: a generative network $\mathcal{G}(\cdot)$ (i.e., generator) that learns the distribution $p_{\text{data}}(\mathbf{x})$ over the data, and a discriminative network $\mathcal{D}(\cdot)$ (i.e., discriminator) that computes the probability that a sample \mathbf{x} is sampled from $p_{\text{data}}(\mathbf{x})$, rather than generated by the generator. The generator maps the low-dimensional latent vector \mathbf{z} from the prior distribution $p(\mathbf{z})$ to the data space. The discriminator is trained to maximize the probability of distinguishing the real samples from the generated (fake) samples. The generator is simultaneously trained to maximally fool the discriminator into assigning a higher probability to the generated samples by leveraging the feedback from the discriminator. Mathematically, the adversarial game translates into the following minimization-maximization loss function (Goodfellow et al., 2014)

$$\min_{\mathcal{G}} \max_{\mathcal{D}} \mathbb{E}_{\mathbf{x} \sim p_{\text{data}}(\mathbf{x})} [\log \mathcal{D}(\mathbf{x})] + \mathbb{E}_{\mathbf{z} \sim p(\mathbf{z})} \left\{ \log [1 - \mathcal{D}[\mathcal{G}(\mathbf{z})]] \right\}. \quad (7)$$

In practice, the generator and discriminator are usually trained in alternating steps: (1) train the discriminator to improve its discriminative capability; (2) train the generator to improve the quality of the generated samples so as to fool the discriminator.

3.3.2 Adversarial Autoencoder

An autoencoder is a framework that learns a low-dimensional representation \mathbf{z} (referred to as latent codes or latent variables) of a sample \mathbf{x} in the data and generates from the codes a reconstruction $\hat{\mathbf{x}}$ that closely matches \mathbf{x} . It consists of two networks: an encoder to learn a mapping from \mathbf{x} to \mathbf{z} and a decoder to learn a mapping from \mathbf{z} to $\hat{\mathbf{x}}$. To create a generative framework, in adversarial autoencoder (Makhzani et al., 2016) a constraint is added on the encoder that forces it to generate latent codes \mathbf{z} that roughly follow a desired distribution, like a standard normal distribution $\mathcal{N}(\mathbf{0}, \mathbf{I})$ used in the present study. The decoder is then trained to generate samples with features being consistent with those found in the training data given any sample $\mathbf{z} \sim \mathcal{N}(\mathbf{0}, \mathbf{I})$ as input, resulting in a generative model.

Mathematically, let $q(\mathbf{z}|\mathbf{x})$ be the encoding distribution, $q(\mathbf{x}|\mathbf{z})$ be the decoding distribution, and $p(\mathbf{z})$ be the distribution that we want the latent variables \mathbf{z} to follow. The adversarial autoencoder looks for a generative model

$$p(\mathbf{x}) = \int p(\mathbf{x}|\mathbf{z})p(\mathbf{z})d\mathbf{z}. \quad (8)$$

The adversarial autoencoder (Makhzani et al., 2016) is very similar to the VAE (Kingma & Welling, 2014) in the sense that in both a latent representation is obtained with a desired distribution. Thus we follow the formulation in VAE to finally introduce the adversarial autoencoder. In VAE, the generative model is obtained via minimizing the upper-bound of the negative log-likelihood

$$\mathbb{E}_{\mathbf{x} \sim p_{\text{data}}(\mathbf{x})} [-\log p(\mathbf{x})] < \mathbb{E}_{\mathbf{x} \sim p_{\text{data}}(\mathbf{x})} \left\{ \mathbb{E}_{\mathbf{z} \sim q(\mathbf{z}|\mathbf{x})} [-\log p(\mathbf{x}|\mathbf{z})] + \text{KL}[q(\mathbf{z}|\mathbf{x})||p(\mathbf{z})] \right\}. \quad (9)$$

The first term on the right side quantifies the reconstruction quality and the second term is the Kullback-Leibler divergence measuring the difference between two distributions.

In adversarial autoencoders, an adversarial training procedure instead of the Kullback-Leibler divergence is used to encourage an aggregated posterior distribution $q(\mathbf{z})$, instead of

$q(\mathbf{z}|\mathbf{x})$, to match $p(\mathbf{z})$, where $q(\mathbf{z})$ is defined as (Makhzani et al., 2016)

$$q(\mathbf{z}) = \int_{\mathbf{x}} q(\mathbf{z}|\mathbf{x})p_{\text{data}}(\mathbf{x})d\mathbf{x}. \quad (10)$$

An illustration of the adversarial autoencoder is depicted in Figure 2a. In the encoding path, the input \mathbf{x} is fed into the encoder which outputs two low-dimensional vectors of means $\boldsymbol{\mu}$ and log-variances $\ln(\boldsymbol{\sigma}^2)$ of the latent variables \mathbf{z} . Then a vector \mathbf{z}' is randomly drawn from $\mathcal{N}(\mathbf{0}, \mathbf{I})$ and rescaled to produce the codes $\mathbf{z} = \boldsymbol{\mu} + \boldsymbol{\sigma} \times \mathbf{z}'$, where \times denotes element-wise multiplication. The decoder takes \mathbf{z} as input to eventually generate $\hat{\mathbf{x}}$. Meanwhile, the discriminator of the adversarial network accepts input from the latent codes generated by the encoder or the prespecified distribution $p(\mathbf{z})$ to discriminatively predict whether the input arises from the encoding codes (fake sample) or $p(\mathbf{z})$ (real sample). Note that the adversarial network here differs slightly from the vanilla GAN framework (Goodfellow et al., 2014), in which the generator generates the sample \mathbf{x} , and the discriminator discriminates \mathbf{x} whether it is from the generator or the data.

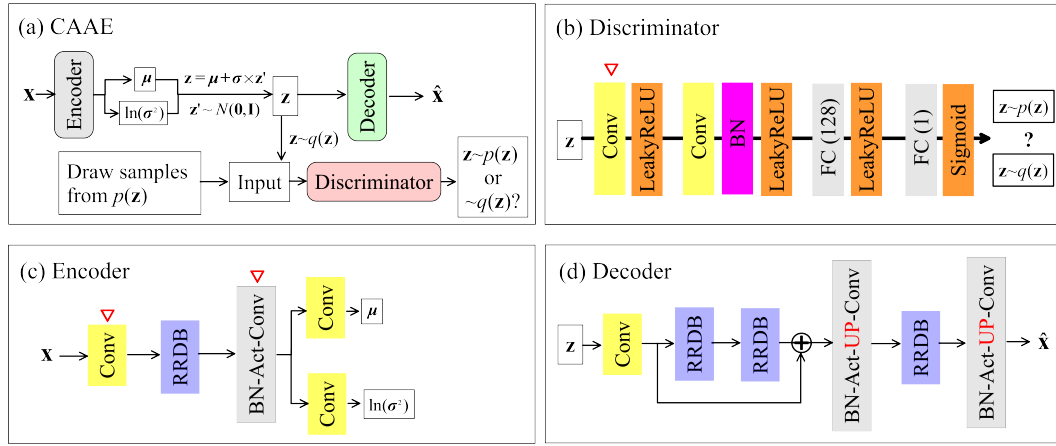


Figure 2: (a) Illustration of a convolutional adversarial autoencoder (CAAE), which is composed of a discriminator (b), an encoder (generator) (c), and a decoder (d). The discriminator is a stack of two convolutional layers followed by two fully-connected (FC) layers with 128 and 1 neurons, respectively. The feature map size is halved in Conv (∇) with stride 2 in the discriminator and encoder, and doubled in the decoder by using the nearest upsampling (UP) operation.

The encoder (which is also the generator $\mathcal{G}(\cdot)$ of the adversarial network), decoder, and discriminator $\mathcal{D}(\cdot)$ of the adversarial autoencoder are trained jointly in two phases for each iteration: the reconstruction phase and the regularization phase (Makhzani et al., 2016). In the reconstruction phase, the encoder (generator) and decoder are updated using the following loss function:

$$\mathcal{L}_{\text{ED}} = \mathcal{L}_{\text{Rec}} + w\mathcal{L}_{\mathcal{G}}, \quad (11)$$

where \mathcal{L}_{Rec} is the reconstruction error which in this study is taken as the L_1 loss:

$$\mathcal{L}_{\text{Rec}} = \frac{1}{N} \sum_{i=1}^N \|\mathbf{x}_i - \hat{\mathbf{x}}_i\|_1, \quad (12)$$

and $\mathcal{L}_{\mathcal{G}}$ measures the generator's ability to fool the discriminator and has the form

$$\mathcal{L}_{\mathcal{G}} = -\frac{1}{N} \sum_{i=1}^N \log \{ \mathcal{D}[\mathcal{G}(\mathbf{x}_i)] \}. \quad (13)$$

Here, w is a weight factor balancing the two losses and a value of $w = 0.01$ is used, $\hat{\mathbf{x}}_i$ is the reconstruction of sample \mathbf{x}_i , and N is the number of training samples. In the regularization phase, the discriminator is updated based on the loss function

$$\mathcal{L}_{\mathcal{D}} = -\frac{1}{N} \sum_{i=1}^N \left\{ \log [\mathcal{D}(\mathbf{z}_i)] + \log [1 - \mathcal{D}(\mathcal{G}(\mathbf{x}_i))] \right\}, \quad (14)$$

to distinguish the real sample from $p(\mathbf{z})$ (i.e. \mathbf{z}_i) from the fake sample $\mathcal{G}(\mathbf{x}_i)$ produced by the generator.

Such adversarial training process with the loss functions defined in equations (11) and (14) forces $\hat{\mathbf{x}}$ to closely match \mathbf{x} and $q(\mathbf{z})$ to gradually approach $p(\mathbf{z})$ (i.e., $\boldsymbol{\mu} \rightarrow \mathbf{0}$ and $\boldsymbol{\sigma}^2 \mathbf{I} \rightarrow \mathbf{I}$), respectively. After training, the decoder will define a generative model $p(\mathbf{x})$ that given an arbitrary input $\mathbf{z} \sim \mathcal{N}(\mathbf{0}, \mathbf{I})$ can generate a new realization of sample $\hat{\mathbf{x}}$ with features similar to those in the data used for training (Figure 2d).

3.3.3 CAAE Networks Based on Residual-in-Residual Dense Blocks

We also adopt the residual-in-residual dense block structure shown in Figure 1b in the encoder and decoder of the CAAE network. The encoder (Figure 2c) is similar to the coarsening part of the DRDCN network (Figure 1c). The encoder has two additional convolutional layers to respectively output the means $\boldsymbol{\mu}$ and log-variances $\ln(\boldsymbol{\sigma}^2)$. The decoder (Figure 2d) is similar to the refining part of the DRDCN network. The decoder has an additional convolutional layer to extract feature maps from the codes \mathbf{z} . The ReLU activation is used in the encoder and decoder. Inspired by Ledig et al. (2017), the discriminator is a stack of two convolutional layers followed by two fully-connected layers with 128 and 1 neurons, respectively. The leaky ReLU activation with a slope of 0.2 is used in the discriminator and the sigmoid activation is used in the last layer to output a probability value between 0 and 1.

3.4 The CAAE-DRDCN-ILUES inversion framework

We incorporate the CAAE parameterization method and the DRDCN surrogate method into ILUES to formulate an efficient inversion scheme for estimation of a non-Gaussian conductivity field of solute transport models. The integrated methodology is denoted as CAAE-DRDCN-ILUES hereinafter and is summarized in Algorithm 2. Notice that in this method, the surrogate model is used in Algorithms 1 and 2 to substitute the forward model. After parameterization, the uncertain parameters to be estimated are the latent variables \mathbf{z} . The log-conductivity field is estimated with the following procedure: (1) start with an initial latent code ensemble drawn from $\mathcal{N}(\mathbf{0}, \mathbf{I})$, (2) the corresponding log-conductivity fields are generated next using the CAAE’s decoder, (3) the surrogate model is evaluated to obtain the predicted initial output ensemble, (4) the latent code and output ensembles are repeatedly updated for N_{iter} iterations using Algorithm 1 based on the current latent code and output ensembles. In Algorithm 1, the input to the surrogate model to produce output predictions is the log-conductivity field, which is generated by the CAAE’s decoder given the latent codes as input. The posterior log-conductivity fields are obtained from the decoder using the last latent code ensemble as input.

4 Application

4.1 Solute Transport Models

The performance of the proposed method is illustrated using 2-D and 3-D solute transport modeling with random conductivity fields that have non-Gaussian heterogeneity patterns.

Algorithm 2 The CAAE-DRDCN-ILUES inversion framework for estimation of the log-conductivity field \mathbf{x} . The log-conductivity field realizations are generated using the CAAE’s decoder given the latent variables \mathbf{z} as input. CAAE: convolutional adversarial autoencoder. DRDCN: deep residual dense convolutional network. ILUES: iterative local updating ensemble smoother.

Require: Measurements \mathbf{d} , iteration number N_{iter} , ensemble size N_e , trained decoder, trained DRDCN.

- 1: Generate the initial input ensemble $\mathbf{Z}^0 = [\mathbf{z}_1^0, \dots, \mathbf{z}_{N_e}^0]$ from $\mathcal{N}(\mathbf{0}, \mathbf{I})$.
 - 2: Generate the initial log-conductivity field ensemble $\hat{\mathbf{X}}^0 = [\hat{\mathbf{x}}_1^0, \dots, \hat{\mathbf{x}}_{N_e}^0]$ via $\hat{\mathbf{x}}_i^0 = \text{decoder}(\mathbf{z}_i^0)$.
 - 3: Obtain the initial output ensemble $\hat{\mathbf{D}}^0 = [\hat{f}(\hat{\mathbf{x}}_1^0), \dots, \hat{f}(\hat{\mathbf{x}}_{N_e}^0)]$ via $\hat{f}(\hat{\mathbf{x}}_i^0) = \text{DRDCN}(\hat{\mathbf{x}}_i^0)$.
 - 4: **for** $n = 0, \dots, (N_{\text{iter}} - 1)$ **do** ▷ Iterative data assimilation
 - 5: Obtain $\mathbf{Z}^{n+1} = [\mathbf{z}_1^{n+1}, \dots, \mathbf{z}_{N_e}^{n+1}]$ and $\hat{\mathbf{D}}^{n+1} = [\hat{f}(\hat{\mathbf{x}}_1^{n+1}), \dots, \hat{f}(\hat{\mathbf{x}}_{N_e}^{n+1})]$ based on $\{\mathbf{Z}^n, \hat{\mathbf{D}}^n, \mathbf{d}\}$ using Algorithm 1.
 - 6: **end for**
 - 7: $\hat{\mathbf{X}}^{N_{\text{iter}}} = [\hat{\mathbf{x}}_1^{N_{\text{iter}}}, \dots, \hat{\mathbf{x}}_{N_e}^{N_{\text{iter}}}]$, where $\hat{\mathbf{x}}_i^{N_{\text{iter}}} = \text{decoder}(\mathbf{z}_i^{N_{\text{iter}}})$.
 - 8: **return** $\hat{\mathbf{X}}^{N_{\text{iter}}}, \hat{\mathbf{D}}^{N_{\text{iter}}}$ ▷ The final log-conductivity field and output ensembles
-

4.1.1 2-D Model

The first test case considers 2-D solute transport within a channelized aquifer. As shown in Figure 3a, the horizontal domain has a size of 10 (L) \times 20 (L) and is uniformly discretized into $H \times W = 40 \times 80 = 3,200$ gridblocks. The left and right boundaries are assumed to be constant head boundaries with heads of 1 (L) and 0 (L), respectively. No-flow boundary condition is imposed on the upper and lower boundaries. An instantaneous source with a concentration of 100 (ML^{-3}) is released from the location $x = 3$ (L) and $y = 5$ (L) at the initial time. The porosity and dispersivities are assumed to be known with constant values of $\phi = 0.25$, $\alpha_L = 1.0$ (L) and $\alpha_T = 0.1$ (L), respectively.

The non-Gaussian conductivity field in this case has a channelized and bimodal pattern with heterogeneous conductivity within each facies. The conductivity realizations are generated by the following procedure: First, a binary facies field is generated using the SNESIM code (Strebelle, 2002) with a training image shown in Figure 3c; then we populate each facies with log-conductivity values from two independently generated Gaussian random fields with a L_2 norm exponential covariance function:

$$C(\mathbf{s}, \mathbf{s}') = \sigma_{\log(K)}^2 \exp \left(-\sqrt{\left(\frac{s_1 - s'_1}{\lambda_1}\right)^2 + \left(\frac{s_2 - s'_2}{\lambda_2}\right)^2} \right), \quad (15)$$

where $\mathbf{s} = (s_1, s_2)$ and $\mathbf{s}' = (s'_1, s'_2)$ denote two arbitrary spatial locations, $\sigma_{\log(K)}^2$ is the variance, and λ_1 and λ_2 are the correlation lengths along the x - and y -axes, respectively. The means of Gaussian random fields corresponding to the high-conductivity channels and the low-conductivity non-channel medium are 4 and 0, respectively, while their variances and correlation lengths are taken the same with $\sigma_{\log(K)}^2 = 0.5$, $\lambda_1 = 4$ (L), and $\lambda_2 = 2$ (L).

4.1.2 3-D Model

The second test case considers solute transport in a 3-D confined aquifer with a size of 1.5 (L) \times 10 (L) \times 20 (L) as depicted in Figure 3d. The domain is uniformly discretized into $D \times H \times W = 6 \times 32 \times 64 = 12,288$ gridblocks. Similar to the 2-D case, the left and right boundaries are assumed to be constant head boundaries with heads of 1 (L) and 0 (L), respectively. No-flow boundary condition is imposed on the boundaries in the direction perpendicular to the y -axis. An instantaneous source with a concentration of 100 (ML^{-3})

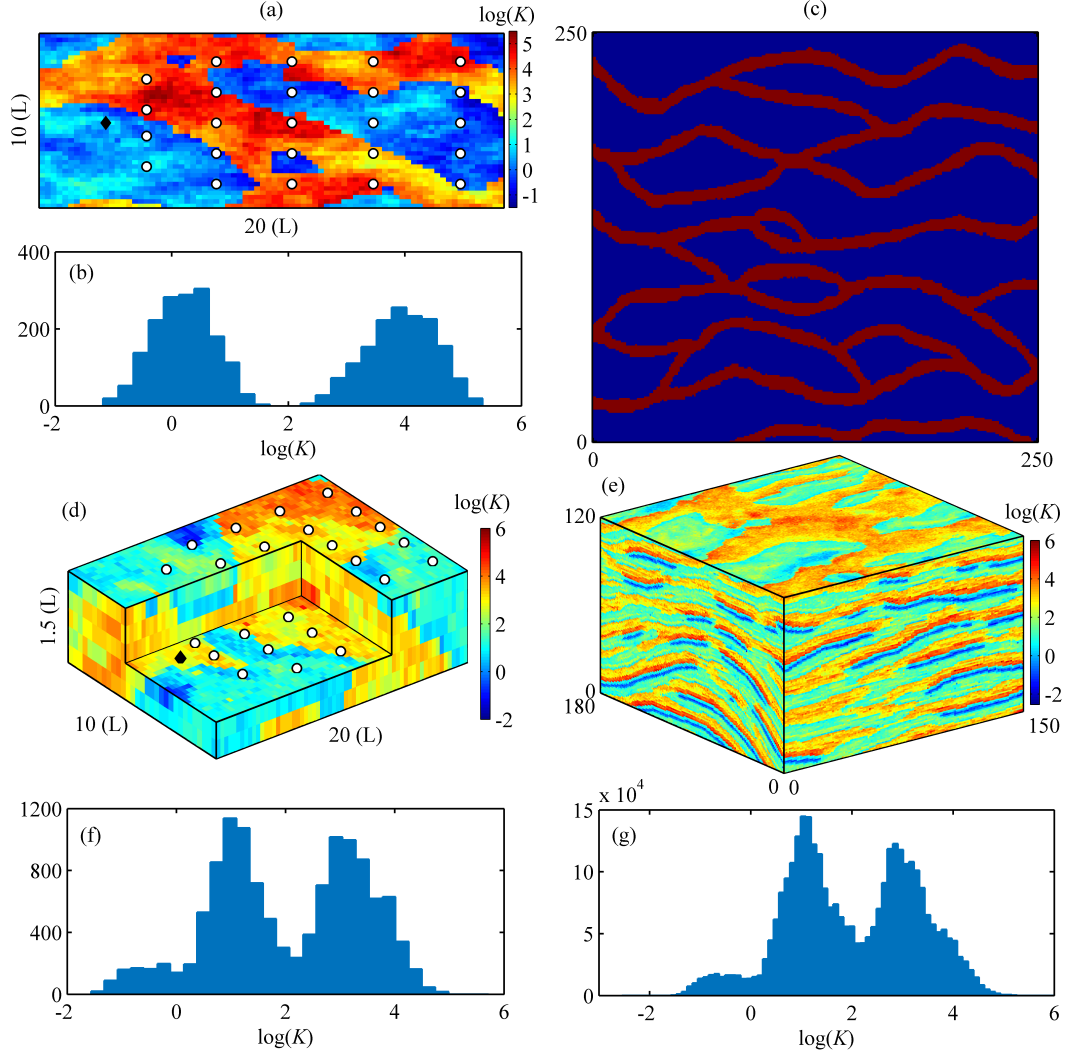


Figure 3: Reference log-conductivity conductivity fields of the 2-D (a) and 3-D (d) solute transport models considered in the inverse problems. The diamond and 24 circles represent the projections of the solute source and observation locations, respectively, in the horizontal plane. Histograms of the log-conductivities in (a) and (d) are shown in (b) and (f), respectively. (c) The 250×250 training image used to generate 2-D binary facies fields. (e) The $120 \times 180 \times 150$ training image used to generate 3-D log-conductivity fields. (g) Histogram of the log-conductivities in (e).

is released from the location $x = 3$ (L) and $y = 5$ (L) at the initial time. The porosity and dispersivities are assumed to be known with constant values of $\phi = 0.25$, $\alpha_L = 1.0$ (L), $\alpha_T = 0.1$ (L), and $\alpha_V = 0.01$ (L), respectively. The conductivity fields for this 3-D model are obtained by randomly cropping $6 \times 32 \times 64$ patches from a $120 \times 180 \times 150$ training image depicted in Figure 3e (available at <http://www.trainingimages.org/training-images-library.html>). The conductivity heterogeneity pattern is different from that in the 2-D channelized field in the sense that the distribution of log-conductivities in this training image is trimodal with two major peaks around 1.0 and 3.0 and one minor peak around -0.6 (Figure 3g).

4.2 Synthetic Observations

As it will be shown in section 5.1, the CAAE-generated conductivity fields have higher regularity/smoothness than the original fields. In the inverse problem, the synthetic observations were obtained by running the forward model with an original conductivity field rather than a smoothed conductivity field generated by CAAE. The generation of synthetic observations here aims to mimic a real scenario, where data would be obtained by field measurements. The randomly generated 2-D and 3-D reference log-conductivity fields are depicted in Figures 3a and 3d, respectively. Note that they are distinct from the training log-conductivity samples of CAAE and DRDCN networks. The two reference fields are both non-Gaussian with a bimodal distribution (the 2-D case, Figure 3b) and a trimodal distribution (the 3-D case, Figure 3f), respectively. In the 2-D case, the concentration at $t = [3, 5, 7, 9, 11]$ (T) and the hydraulic head are collected at 24 measurement locations (Figure 3a), resulting in 144 observations. In the 3-D case, the concentration at $t = [4, 6, 8]$ (T) and the hydraulic head are collected at six depths of 24 measurement locations (Figure 3d), resulting in 576 observations. The synthetic observations were corrupted with 5% independent Gaussian random noise to the data generated by the reference model. Additionally, we do not use any conditioning data (i.e., measurements) of the conductivity, resulting in a rather challenging inverse problem.

4.3 Networks Design and Training

4.3.1 CAAE Network Design and Training

The architecture of the CAAE network is shown in Figure 2 and detailed in section 3.3.3. The encoder includes two downsampling layers which halves the feature map size via convolution with a stride of 2. Correspondingly, the two upsampling layers in the decoder double the feature map size to recover the output image size. The network consists of 71 layers, including 69 convolutional layers (mostly arising from the four residual-in-residual dense blocks that each contains 15 convolutional layers) and 2 fully-connected layers (in the discriminator). The kernel size in all convolutional layers is 3, and the stride in the convolutional layers that keep the same feature map size and halve the size is 1 and 2, respectively.

In the 2-D case, a training set with 40,000 realizations of the log-conductivity field is generated. We also generate another 4,000 test realizations to evaluate the network’s performance. In the 3-D case, we generate the log-conductivity realizations by cropping the $120 \times 180 \times 150$ training image shown in Figure 3e. The original training image is split into two images, with the lower $105 \times 180 \times 150$ part and the upper $15 \times 180 \times 150$ part being used to generate the training and test datasets, respectively. The two images are both flipped along the three dimensions via the `flip` operation implemented in MATLAB to augment the data, each resulting in four training images. The log-conductivity realizations with size $6 \times 32 \times 64$ are then generated via cropping the training images using a stride of (2, 6, 10). In this way, we obtain 37,600 training samples and 3,000 test samples. The data augmentation strategy, which artificially creates new training data from existing training data via specific operations (e.g., flip, shift, and rotation), is commonly utilized to obtain improved performance (Krizhevsky et al., 2012). Note that these operations may lead to correlation between the original and resulting samples, thus the training and test data are generated separately as mentioned above to avoid potential over-optimistic results when assessing the performance. The reference log-conductivity fields used in section 4.2 to generate the synthetic observations are randomly selected from the test sets. The loss functions for network training are defined in equations (11) and (14). The network is trained on a NVIDIA GeForce GTX 1080 Ti X GPU for 50 epochs using the Adam optimizer (Kingma & Ba, 2014) with a learning rate of 2×10^{-4} and a batch size of 64. The training required about 1.7 h and 13.1 h in the 2-D and 3-D cases, respectively.

4.3.2 DRDCN Network Design and Training

The architecture of the DRDCN network is shown in Figure 1 and detailed in section 3.2.2. The network is fully-convolutional and contains 64 convolutional layers without any fully-connected layers. The kernel size in all convolutional layers is 3, and the stride in the convolutional layers that keep the same feature map size and halve the size is 1 and 2, respectively. The softplus activation is used in the output layer for the concentration to ensure nonnegative predictions. Since the hydraulic head varies between 0 and 1 in both cases, the sigmoid activation is used in the output layer for the hydraulic head.

The concentration at different time steps (i.e., $t = [3, 5, 7, 9, 11]$ (T) and $t = [4, 6, 8]$ (T) in the 2-D and 3-D cases, respectively) and the hydraulic head are collected as the observations in the inverse problem. Thus, the concentration fields at these time steps and the hydraulic head field are treated as the output channels of the network. There is one single input channel to the network which is the original log-conductivity field generated by following the procedure presented in section 4.1. In both cases, we generate four training sets with $N = 1,000, 2,000, 3,000,$ and $4,000$ samples to evaluate the convergence of the network approximation errors with respect to the training sample size. The approximation accuracy is assessed using $N_{\text{test}} = 1,000$ randomly generated test samples. Note that since the 3-D log-conductivity realizations are obtained via cropping the training image which may lead to data correlation issue (see section 4.3.1), the log-conductivity samples in the training and test data are randomly selected from the training and test datasets of the CAAE network, respectively. The accuracy is measured using the coefficient of determination (R^2), the root-mean-square error (RMSE), and the structural similarity index (SSIM) metrics. The R^2 and RMSE metrics are defined as

$$R^2 = 1 - \frac{\sum_{i=1}^{N_{\text{test}}} \|\mathbf{y}_i - \hat{\mathbf{y}}_i\|_2^2}{\sum_{i=1}^{N_{\text{test}}} \|\mathbf{y}_i - \bar{\mathbf{y}}\|_2^2}, \quad (16)$$

and

$$\text{RMSE} = \sqrt{\frac{1}{N_{\text{test}}} \sum_{i=1}^{N_{\text{test}}} \|\mathbf{y}_i - \hat{\mathbf{y}}_i\|_2^2}, \quad (17)$$

respectively, where \mathbf{y} denotes the simulated outputs, $\hat{\mathbf{y}}$ is the network predictions, and $\bar{\mathbf{y}} = 1/N_{\text{test}} \sum_{i=1}^{N_{\text{test}}} \mathbf{y}_i$. The SSIM metric measures the structural similarity between two images (fields) and is calculated over local windows of the image (Z. Wang et al., 2004)

$$\text{SSIM}(\mathbf{u}, \mathbf{v}) = \frac{(2\mu_{\mathbf{u}}\mu_{\mathbf{v}} + c_1)(2\sigma_{\mathbf{uv}} + c_2)}{(\mu_{\mathbf{u}}^2 + \mu_{\mathbf{v}}^2 + c_1)(\sigma_{\mathbf{u}}^2 + \sigma_{\mathbf{v}}^2 + c_2)}, \quad (18)$$

where \mathbf{u} and \mathbf{v} are two windows with size 11×11 in the real and predicted images, respectively, $\mu_{\mathbf{u}}$ ($\mu_{\mathbf{v}}$) and $\sigma_{\mathbf{u}}^2$ ($\sigma_{\mathbf{v}}^2$) are the mean and variance values of window \mathbf{u} (\mathbf{v}), $\sigma_{\mathbf{uv}}$ denotes the covariance between \mathbf{u} and \mathbf{v} , and $c_1 = 0.01$ and $c_2 = 0.03$ are two constants (Z. Wang et al., 2004). Note that the SSIM metric is designed for 2-D images. A 3-D image with size $D \times H \times W$ is treated as D images with size $H \times W$ when computing the SSIM metric. A R^2 score value and a SSIM value approaching 1.0 and a lower RMSE value suggest better surrogate quality.

The network is trained using a regularized L_1 loss function:

$$\mathcal{L} = \frac{1}{N} \sum_{i=1}^N \|\mathbf{y}_i - \hat{\mathbf{y}}_i\|_1 + \frac{w_d}{2} \boldsymbol{\theta}^\top \boldsymbol{\theta}, \quad (19)$$

where $\boldsymbol{\theta}$ denotes all the network trainable parameters and $w_d = 1 \times 10^{-5}$ is a regularization coefficient. The network is trained on a NVIDIA GeForce GTX 1080 Ti X GPU for 200 epochs in the 2-D case and 300 epochs in the 3-D case using the Adam optimizer (Kingma & Ba, 2014) with an initial learning rate of 5×10^{-3} and a batch size of 32. We also use a learning rate scheduler which drops ten times on plateau during training. The training required about 0.3-1.2 h and 2.5-10.5 h in the 2-D and 3-D cases, respectively, as the training set size varies from 1,000 to 4,000.

5 Results and Discussion

In this section, we first illustrate the performance of the CAAE and DRDCN networks in parameterization of non-Gaussian random fields and in surrogate modeling of the solute transport models, respectively. After that, the inversion results obtained from the CAAE-DRDCN-ILUES framework are compared to those obtained from the CAAE-ILUES framework without surrogate modeling.

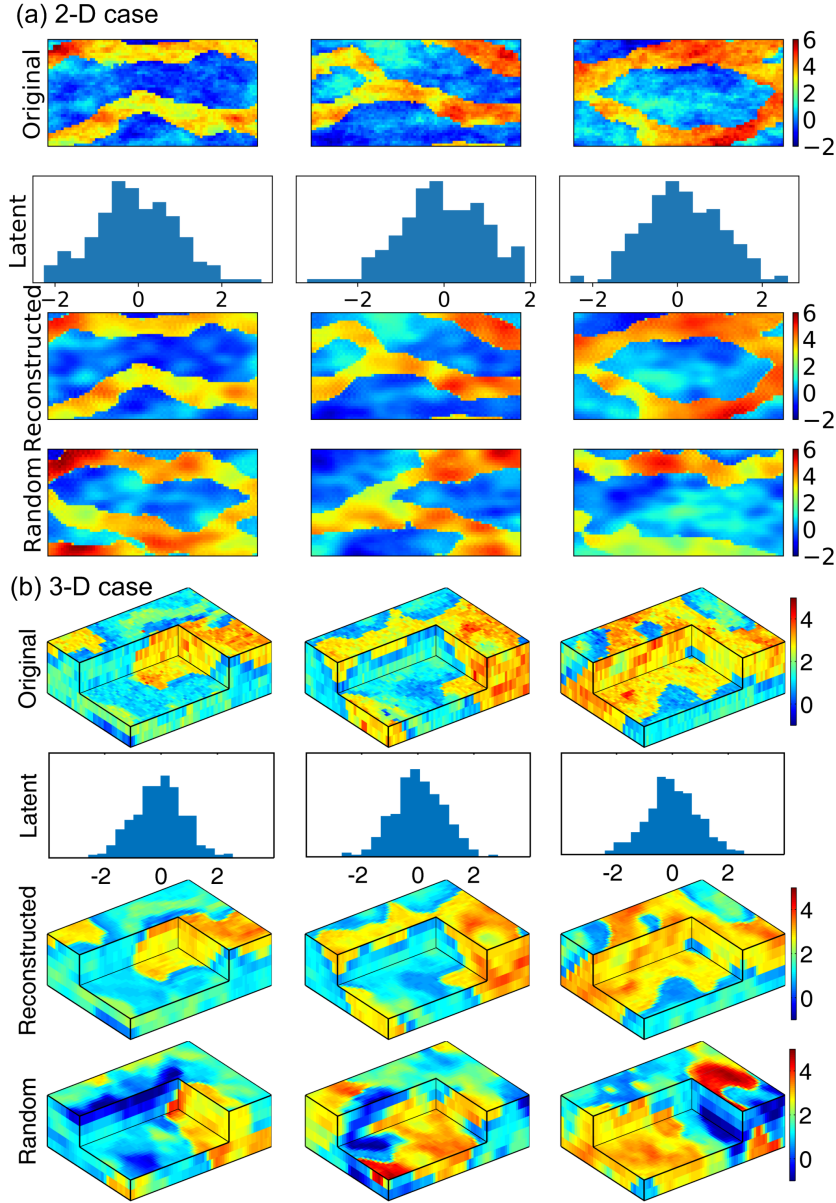


Figure 4: The CAAE network's reconstructions (row 3) for 2-D (a) and 3-D (b) log-conductivity fields (row 1) in the test sets and the corresponding histograms of the latent codes (row 2). The reconstruction accuracy in (a) and (b) is $R^2 = (0.945, 0.948, 0.944)$ and $(0.854, 0.837, 0.852)$, respectively. The fourth row in (a) and (b) shows random log-conductivity fields generated by the CAAE's decoder with inputs from $\mathcal{N}(\mathbf{0}, \mathbf{I})$.

5.1 Parameterization of Non-Gaussian Random Fields

In the CAAE network, the latent dimensions in the 2-D and 3-D cases are set to 200 and 512, respectively. The parameterization results for non-Gaussian log-conductivity fields are shown in Figure 4. It depicts the CAAE’s reconstructions of three log-conductivity realizations in the test set, the corresponding histograms of the latent codes, and three random log-conductivity fields generated by the decoder with inputs from $\mathcal{N}(\mathbf{0}, \mathbf{I})$. In the reconstruction process, the original log-conductivity realization is fed to the encoder to produce latent codes, based on which the reconstructed field is generated by the decoder. It is observed that, in both 2-D and 3-D cases with different heterogeneity patterns, the network successfully recovers the spatial distributions of the low-conductivity and high-conductivity regions as well as the conductivities within these regions; although the conductivity heterogeneity is smoothed compared to the original fields. This heterogeneity smoothness is attributed to the information loss during the encoding and decoding processes. The encoding latent codes roughly follow the prior distribution $\mathcal{N}(\mathbf{0}, \mathbf{I})$ that we imposed during training. The reconstruction accuracy evaluated on the test sets is $R^2 = 0.945$ and 0.863 in the 2-D and 3-D cases, respectively. A larger latent dimension can be used in order to preserve more heterogeneity features in the generated fields, which however may lead to higher computational costs in inverse problems. The fourth row of Figures 4a and 4b shows the random log-conductivity fields generated by the decoder. The results show that the decoder is able to reproduce log-conductivity realizations that depict similar patterns of heterogeneity (e.g., the channel structures and the conductivity continuity within the low/high-conductivity regions) to those found in the training data. Therefore, the CAAE network is employed in the inversion process as the parameterization framework for non-Gaussian conductivity fields.

5.2 Surrogate Quality Assessment

To illustrate the superior performance of the proposed DRDCN network architecture against the DDCN network architecture employed in our previous studies (Mo, Zabararas, et al., 2019; Mo, Zhu, et al., 2019; Zhu & Zabararas, 2018; Zhu et al., 2019) for surrogate modeling of systems with highly-complex input-output mappings, the DDCN network is also trained using the same training sets as those used in DRDCN. The DDCN network architecture is introduced in Appendix A.

The two networks’ approximation accuracy for the 2-D and 3-D solute transport models is provided in Figure 5, which depicts the RMSEs, R^2 scores, and SSIMs evaluated on the test sets. It can be seen that DRDCN achieves lower RMSEs, higher R^2 scores, and overall higher SSIMs than DDCN when being trained using the same four training sets in both cases. For example, with 4,000 training samples, our network achieves a RMSE of 0.016, a R^2 score of 0.972, and a median SSIM value of 0.994 in the 2-D case, while those obtained by the DDCN network are 0.024, 0.933, and 0.978, respectively (Figures 5a and 5c). This implies that the DRDCN network can obtain accurate surrogates with fewer training samples (forward model runs) than the DDCN network. For instance, the 2-D DRDCN surrogate with 2,000 training samples results in approximation accuracy comparable to that of the DDCN surrogate with 5,000 training samples (thus with 50% reduction in training samples). The saved number of training samples indicates substantial computational gains especially for computationally intensive forward models in subsurface modeling where one single model execution can take up to hours or even days. The R^2 scores of the DRDCN networks for the concentration fields at different time steps and the hydraulic head field are depicted in Figures 5e and 5f. It is observed that the approximation accuracy for the hydraulic head is higher than that for the concentration. This is mainly because the hydraulic head is less sensitive to the conductivity heterogeneity compared to the concentration (Kitanidis, 2015), leading to relatively smooth hydraulic fields that are easier-to-approximate. In addition, there is no significant difference between the approximation accuracy for the concentration fields at different time steps. The DRDCN network’s predictions for the output fields of 2-D and 3-D models given randomly selected input log-conductivity fields in the test sets are

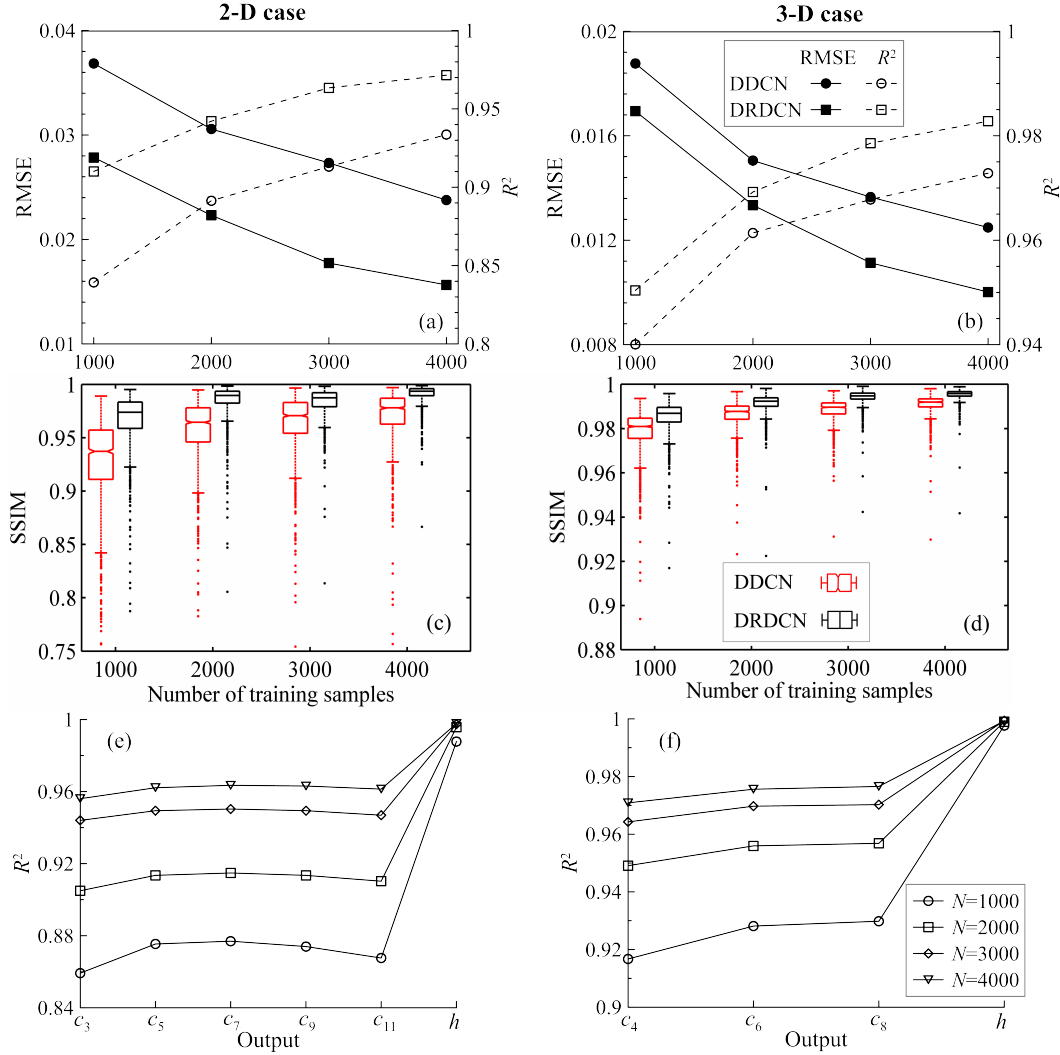


Figure 5: Comparison of the RMSEs, R^2 scores, and SSIMs of the DDCN and DRDCN networks evaluated on the test sets of the 2-D (left column) and 3-D cases (right column). The boxplots summarize the SSIM values evaluated on all output fields in the test sets. The metrics in (a-d) evaluate the approximation accuracy for the concentration field at all time steps considered and the hydraulic head field. (e) and (f) compare the R^2 scores of the DRDCN networks for the concentration (c_t) fields at different time t (T) and the hydraulic head (h) field when trained using different numbers (N) of samples.

illustrated in Figures 6 and 7, respectively. For comparison, the predictions by the forward models and network approximation errors are also shown in each plot. It is observed that although the output fields are highly irregular with sharp response changes, our network is able to obtain good approximations in both cases.

It is worth noticing that the DRDCN network achieves higher accuracy improvement compared to the DDCN network in the 2-D case than in the 3-D case (Figure 5). The low-conductivity regions are barriers for groundwater flow and solute transport, leading to irregular output fields. In comparison to the 2-D log-conductivity fields which are mainly composed of low-conductivity regions (Figure 3c), the facies with the minimum average log-conductivity in the trimodal 3-D fields (i.e., the blue regions in Figure 3e) is only a

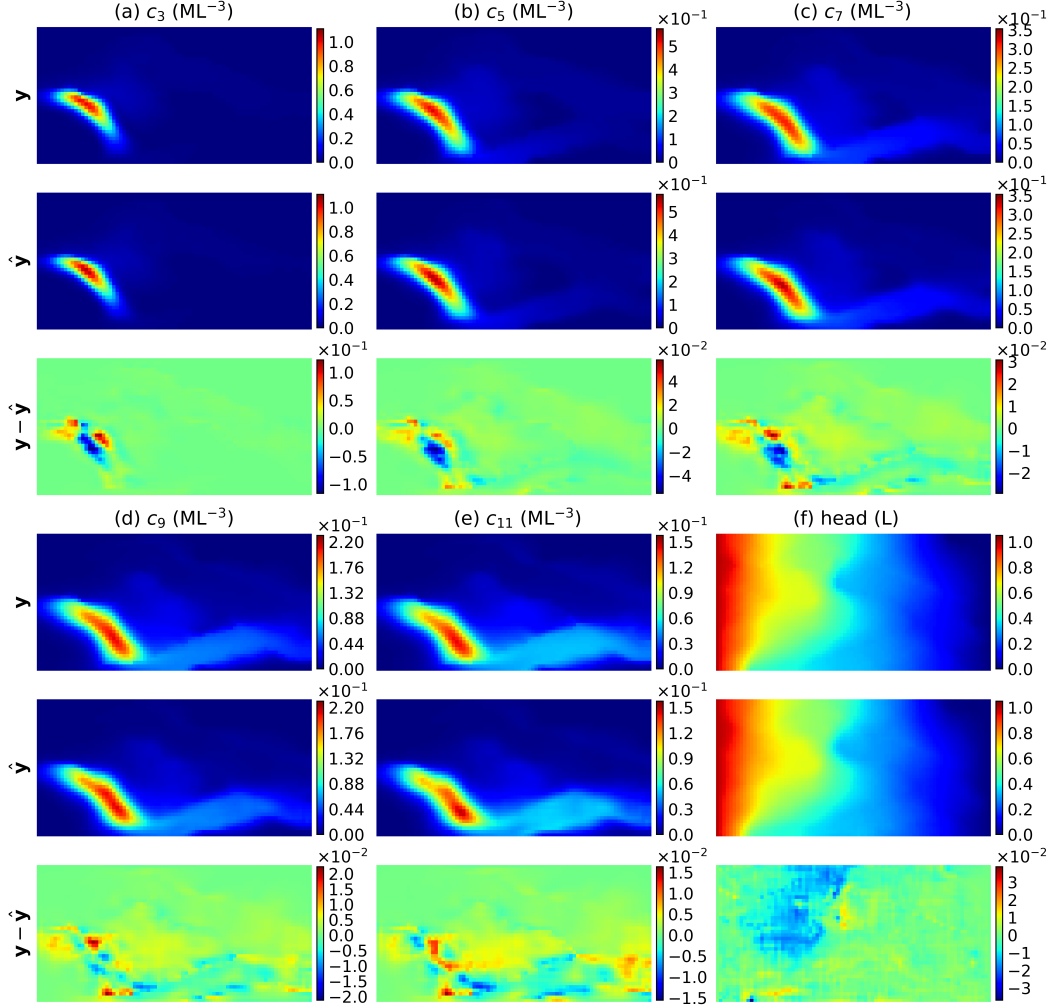


Figure 6: Comparison of the concentration (c_t) fields at time $t = [3, 5, 7, 9, 11]$ (T; a-e) and the hydraulic head field (f) of a random test sample predicted by the 2-D forward model (\mathbf{y}) and the DRDCN network ($\hat{\mathbf{y}}$) trained using 4,000 samples. ($\mathbf{y} - \hat{\mathbf{y}}$) denotes the network approximation error.

small proportion of the aquifer as indicated in Figure 3g. The small proportion of low-conductivity regions in the 3-D fields thus results in relatively smoother output fields than those of the 2-D model. As a consequence, the DDCN network can also obtain a relatively accurate surrogate of the 3-D model, although its approximation error is larger than that of the DRDCN network. However, its performance greatly decreases in the 2-D model with more complex output fields. The results clearly suggest that the proposed DRDCN network performs better than the DDCN network in obtaining accurate surrogate results for the solute transport models with high-dimensional and highly-complex input-output relations. The improvement is attributed to the deeper network architecture with the help of the multilevel residual learning (X. Wang et al., 2018) and residual scaling strategies (Szegedy et al., 2016). With a relatively small number of training samples, the DRDCN network is able to provide good approximations of the 2-D and 3-D forward models. Thus, it is used together with the CAAE parameterization strategy in the ILUES inverse method to formulate an efficient inversion framework for estimation of a non-Gaussian conductivity field of solute transport models.

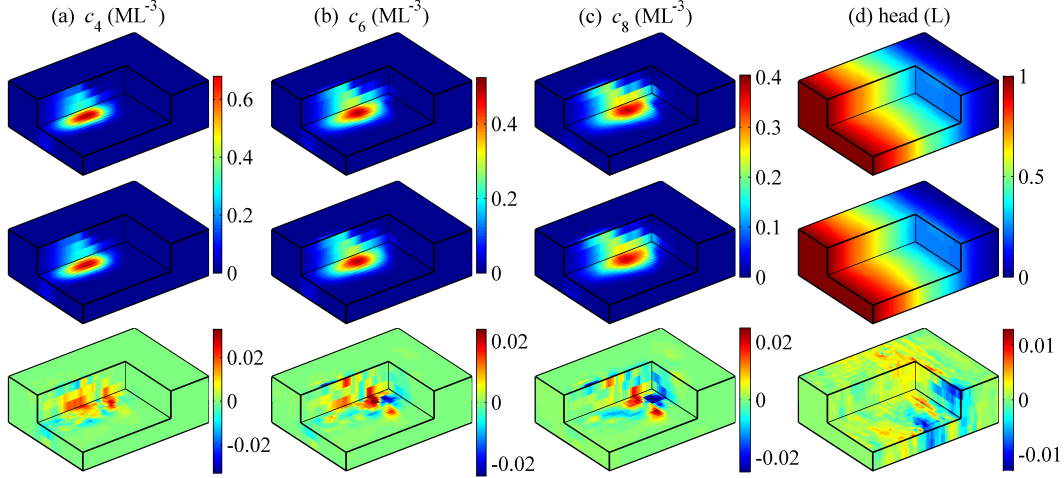


Figure 7: Comparison of the concentration (c_t) fields at time $t = [4, 6, 8]$ (T; a-c) and the hydraulic head field (d) of a random test sample predicted by the 3-D forward model (\mathbf{y}) and the DRDCN network ($\hat{\mathbf{y}}$) trained using 4,000 samples. ($\mathbf{y} - \hat{\mathbf{y}}$) denotes the network approximation error.

5.3 Inversion Results

In both 2-D and 3-D cases, the DRDCN surrogates trained with 4,000 forward model runs are used to substitute the forward models in the CAAE-DRDCN-ILUES inversion framework. To assess the accuracy and computational efficiency of the surrogate-based method, the CAAE-ILUES method which evaluates the forward model rather than the surrogate model during the inversion is also performed. The ensemble size of the ILUES algorithm is set to $N_e = 2,000$ and $N_e = 3,000$ in the 2-D and 3-D cases, respectively, to fully quantify the parametric uncertainty. The observations are assimilated for $N_{\text{iter}} = 30$ iterations in the 2-D case and 20 iterations in the 3-D case. That is, the number of forward model runs required in CAAE-ILUES for the 2-D and 3-D cases are $31 \times 2,000 = 62,000$ (i.e., one prior ensemble and N_{iter} updated ensembles) and $21 \times 3,000 = 63,000$, respectively. The posterior log-conductivity fields are then obtained from the CAAE's decoder given the final latent code ensemble as input (Algorithm 2).

The convergence of the fitting error between the model predictions and measurements as the iteration proceeds is shown in Figure 8, where the mismatch is measured using the normalized sum of squared weighted residuals ($NSSWR$):

$$NSSWR = \frac{1}{SSWR_{\text{ref}}} \sum_{i=1}^{N_d} \left(\frac{f_i(\hat{\mathbf{x}}) - d_i}{\sigma_i} \right)^2, \quad (20)$$

where $\{d_i\}_{i=1}^{N_d}$ denote the measurements that contain measurement errors with standard deviations $\{\sigma_i\}_{i=1}^{N_d}$, and $\{f_i(\hat{\mathbf{x}})\}_{i=1}^{N_d}$ are the forward model predictions given the input $\hat{\mathbf{x}}$ which is generated by the decoder. Here the $SSWR$ metric is normalized using the reference value $SSWR_{\text{ref}}$. Thus, a $NSSWR$ value approaching 1.0 suggests the convergence of the inversion process. As discussed in sections 4.2 and 5.1, the reference log-conductivity field has high heterogeneity versus the smoothed CAAE-parameterized field realizations $\hat{\mathbf{x}}$. As a consequence, in the inversion process the $NSSWR$ values are not able to converge to the reference $NSSWR$ value (i.e., 1.0) due to the conductivity smoothness in the CAAE-generated samples. This can be seen in Figure 8 where although the $NSSWR$ values in the ensemble approximately converge in both cases, the converged values (the mean values are 1.68 and 2.17 in the 2-D and 3-D cases, respectively) are larger than 1.0. Our tests

showed that the $NSSWR$ values were not able to converge asymptotically to 1.0 even when we increased the number of iterations in ILUES. The results of CAAE-DRDCN-ILUES are also shown in Figure 8 (the surrogate prediction $\hat{f}(\cdot)$ is used in equation (20)). This method converges to larger $NSSWR$ values (the mean values are 2.95 and 2.19 in the 2-D and 3-D cases, respectively) mainly due to the approximation errors of the DRDCN surrogate model. Accounting for the approximation errors in the inversion is expected to further improve the estimation accuracy (Cui et al., 2011; J. Zhang et al., 2016). This can be realized by building a model for the approximation errors and then accounting for the approximation error contribution to the covariance matrix \mathbf{C}_D (Cui et al., 2011). Alternatively, one can employ a Bayesian training strategy (e.g., Stein variational gradient descent (Q. Liu & Wang, 2016)) for the DRDCN network as in Zhu and Zabaras (2018), which can provide multiple sets of tuned network parameters and thus an estimation of the variance in the prediction. The uncertainty estimate can subsequently be incorporated in \mathbf{C}_D as in J. Zhang et al. (2016) to alleviate the influence of approximation errors. The training of Bayesian networks, however, is more expensive than that of non-Bayesian networks (Zhu & Zabaras, 2018).

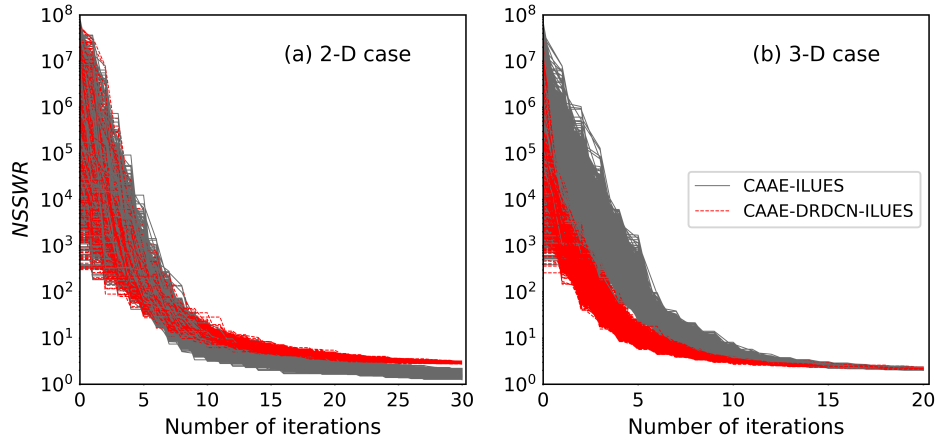


Figure 8: Convergence of the $NSSWR$ values in the ensembles of CAAE-ILUES and CAAE-DRDCN-ILUES as the number of iterations increases.

Two posterior log-conductivity realizations, the ensemble mean, ensemble standard deviation, and histogram of the log-conductivities in the ensemble mean field of the CAAE-ILUES method for the two cases are illustrated in Figure 9. The reference fields and the locations of the output measurements collected to infer the conductivity field are also shown in the plot to facilitate the comparison. It can be seen that in both cases the CAAE-ILUES can successfully capture the spatial distribution of the high-conductivity and low-conductivity regions as well as the conductivities within these regions. This is also indicated by the multimodal distribution of the log-conductivities in the mean fields. Due to the relatively sparse measurements (i.e., only 24 observation wells are placed in the domain with thousands of gridblocks), the local conductivity heterogeneity, the location of the boundaries between high-conductivity and low-conductivity regions, the mean values of the modes in the histograms may not be accurately retrieved. As expected, the conductivity estimation in regions where no information is collected is less accurate with a larger estimation uncertainty than the estimation near the the output measurement locations. The results imply that the CAAE-ILUES algorithm performs well for this inverse problem but needs a large number of forward model evaluations. We show next the results of CAAE-DRDCN-ILUES in which the DRDCN surrogate models are used to substitute the 2-D and 3-D forward models. Various statistics for the same reference fields as in CAAE-ILUES are depicted in the third row of

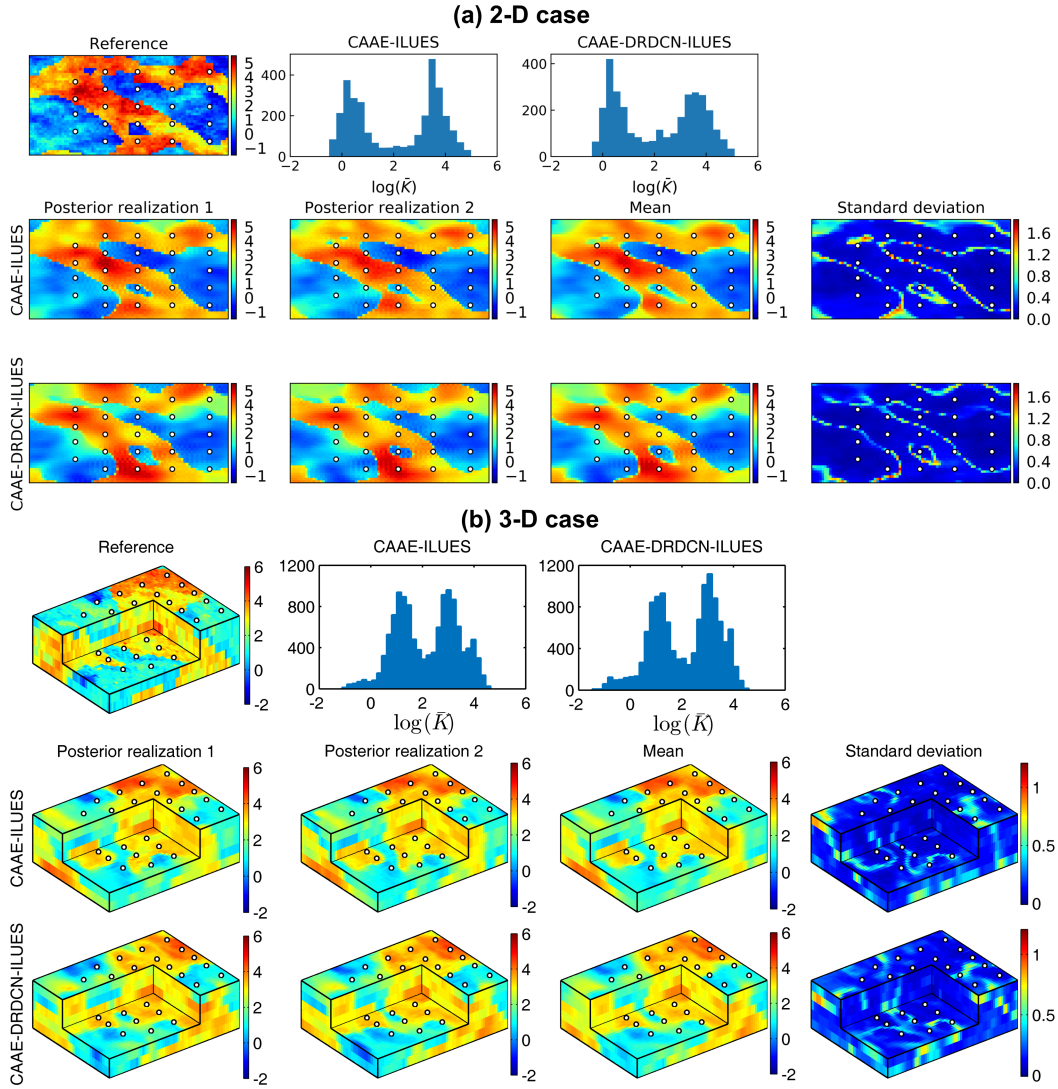


Figure 9: Two posterior log-conductivity realizations, ensemble mean, and ensemble standard deviation obtained from the CAAE-ILUES and the CAAE-DRDCN-ILUES methods. The histograms are for the mean log-conductivity values ($\log(\bar{K})$) of all posterior realizations. The reference fields shown in (a) and (b) are those in Figures 3a and 3d, respectively. The circles denote the projections of the output measurement locations on the horizontal plane.

Figures 9a (2-D case) and 9b (3-D case). Similarly, it can be seen that in both cases the surrogate-based framework successfully captured the multimodal features and identified the high-conductivity and low-conductivity regions as well as the conductivities within these regions.

Figures 10 and 11 show the output ensemble mean and standard deviation estimates of the CAAE-ILUES and CAAE-DRDCN-ILUES methods for the 2-D and 3-D models, respectively. The reference output fields and the observation locations are also shown to facilitate the analysis of results. Notice that the statistics of the surrogate-based method are computed using the outputs predicted by the surrogate model rather than the forward model. It can be observed that the CAAE-DRDCN-ILUES method achieves similar ensemble mean

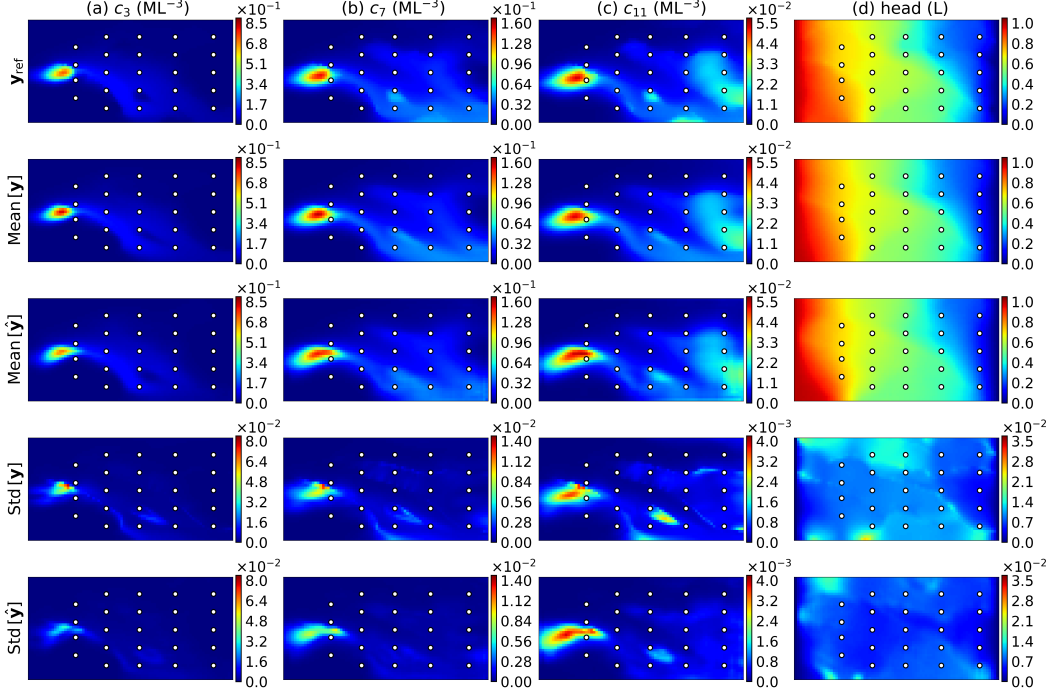


Figure 10: Ensemble mean and standard deviation (Std) of the concentration (c_t) fields at time $t = [3, 7, 11]$ (T; a-c) and hydraulic head field (d) of the 2-D model obtained from CAAE-ILUES (Mean[\mathbf{y}], Std[\mathbf{y}]) and CAAE-DRDCN-ILUES (Mean[$\hat{\mathbf{y}}$], Std[$\hat{\mathbf{y}}$]). \mathbf{y}_{ref} denotes the output fields of the reference model with the log-conductivity field shown in Figure 3a. The circles denote the measurement locations.

estimates to those of the CAAE-ILUES method which successfully reproduce the main patterns of the reference output fields in the two cases. Similar to the estimation of the conductivity field, a higher reproduction accuracy and a lower estimation uncertainty are observed near the observation wells than those in regions where no information is collected.

The results indicate that the CAAE network is able to reconstruct well non-Gaussian conductivity fields with different heterogeneity patterns and therefore the CAAE-ILUES method can obtain good inversion results in the 2-D and 3-D cases. However, for the two high-dimensional and highly-nonlinear inverse problems considered here, more than 60,000 forward model runs are needed in each case, leading to a high computational cost. On the contrary, the surrogate-based framework CAAE-DRDCN-ILUES can provide similar inversion results with much less computation costs. To assess the computational efficiency of the surrogate method, let $N_{\text{C-I}}$ and $N_{\text{C-D-I}}$ denote the number of forward model runs needed by CAAE-ILUES and CAAE-DRDCN-ILUES, respectively. Also, the C_f and C_{train} represent the computational cost of one forward model run and of training the surrogate model, respectively. The computation time of the original ($C_{\text{C-I}}$) and surrogate-based ($C_{\text{C-D-I}}$) ILUESs are written as

$$C_{\text{C-I}} = N_{\text{C-I}}C_f, \quad (21)$$

and

$$C_{\text{C-D-I}} = N_{\text{C-D-I}}C_f + C_{\text{train}}, \quad (22)$$

respectively (the training time of CAAE parameterization model is the same for the two methods, thus it is not included in the equations). Thus, $C_{\text{C-I}} = 1.74 \times 10^5$ s and $C_{\text{C-D-I}} = 1.55 \times 10^4$ s in the 2-D case ($N_{\text{C-I}} = 62,000$, $N_{\text{C-D-I}} = 4,000$, $C_f = 2.8$ s, and $C_{\text{train}} =$

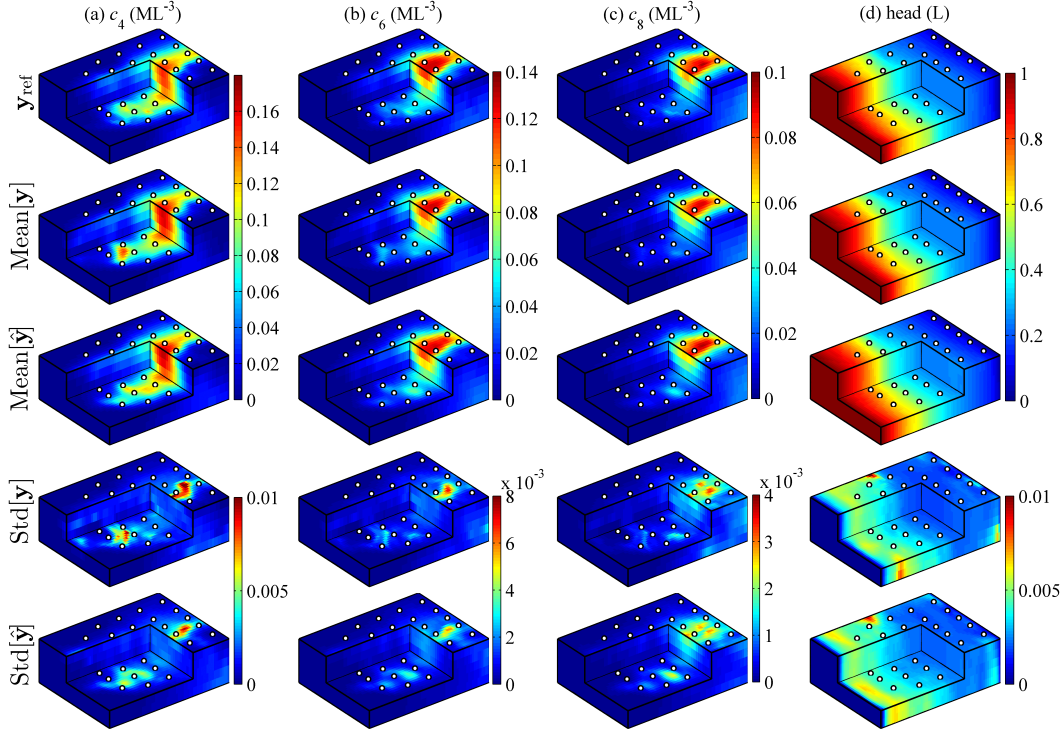


Figure 11: Ensemble mean and standard deviation (Std) of the concentration (c_t) fields at time $t = [4, 6, 8]$ (T; a-c) and hydraulic head field (d) of the 3-D model obtained from CAAE-ILUES (Mean[y], Std[y]) and CAAE-DRDCN-ILUES (Mean[\hat{y}], Std[\hat{y}]). \mathbf{y}_{ref} denotes the output fields of the reference model with the log-conductivity field shown in Figure 3d. The circles denote the projections of the measurement locations on the horizontal plane.

4.32×10^3 s), and $C_{C-I} = 8.25 \times 10^5$ s and $C_{C-D-I} = 9.02 \times 10^4$ s in the 3-D case ($N_{C-I} = 63,000$, $N_{C-D-I} = 4,000$, $C_f = 13.1$ s, and $C_{\text{train}} = 3.78 \times 10^4$ s). The computational savings obtained by the surrogate-based method ($\frac{C_{C-I} - C_{C-D-I}}{C_{C-I}} \times 100\%$) in the 2-D and 3-D cases are both about 90%. When applying the method to computationally more intensive forward models (i.e., when C_f is large), more savings of computation time

$$C_{\text{saving}} = C_{C-I} - C_{C-D-I} = (N_{C-I} - N_{C-D-I})C_f - C_{\text{train}}, \quad (23)$$

can be expected as $N_{C-I} \gg N_{C-D-I}$.

6 Conclusions

In this study, we propose an integrated inversion framework for efficient characterization of solute transport in non-Gaussian conductivity fields with multimodal distributions. In the proposed framework, a CAAE network is developed for parameterization of the conductivity field using a low-dimensional latent representation. In addition, a DRDCN network is developed for surrogate modeling of the solute transport model with high-dimensional and highly-complex input-output mappings. The two networks are combined with the ILUES inversion method (J. Zhang et al., 2018) to formulate the CAAE-DRDCN-ILUES inversion framework. To improve the networks' performance for approximating the highly-complex mappings in the problems considered, in both network architectures, we adopt a multi-level residual learning structure referred to as residual-in-residual dense block (X. Wang et al., 2018). This structure can effectively ease the training process allowing for a large

network depth which has the potential to substantially increase the network’s capability to approximate highly-complex mappings.

The performance of the proposed method is evaluated using 2-D and 3-D solute transport modeling with non-Gaussian conductivity fields that have different patterns of conductivity heterogeneity. The results indicate that the CAAE is capable of representing a non-Gaussian conductivity field using a low-dimensional latent vector, though this is at the cost of the smoothness of local heterogeneity. The DRDCN network shows a superior performance over the DDCN network proposed in our previous studies (Mo, Zabararas, et al., 2019; Mo, Zhu, et al., 2019; Zhu & Zabararas, 2018; Zhu et al., 2019) in obtaining accurate surrogate models. The residual-in-residual dense block structure greatly improves the network’s capacity in approximating highly-complex mappings. The application of the CAAE-DRDCN-ILUES method for estimation of the 2-D and 3-D non-Gaussian conductivity fields shows that it can obtain similar inversion results and predictive uncertainty estimations to those obtained by the original inverse method without surrogate modeling. The integrated method is highly efficient since the training of the surrogate model requires only a small number of forward model runs. The solute transport models considered in this work are relatively fast in order to quickly test the proposed method in a reasonable time. When applying to computationally more intensive forward models, significant computational gains can be expected.

Note that incorporating the surrogate model in the inversion introduces an additional source of uncertainty due to approximation errors. Consideration of these approximation errors in the inversion process can be beneficial in improving the accuracy and reliability of the results (Cui et al., 2011; J. Zhang et al., 2016). To this end, even if not considered or demonstrated herein, one can build a model for the approximation errors (Cui et al., 2011) or employ a Bayesian version of the DRDCN surrogate (Zhu & Zabararas, 2018; Zhu et al., 2019) for estimating the variance in the prediction, so as to incorporate the approximation errors in the inversion formula. In the current work, the presented methods were demonstrated using synthetic problems. Their potential use in practical applications and other complex systems beyond groundwater solute transport deserves further exploration due to their data-driven and nonintrusive nature.

Acknowledgments

S.M. acknowledges partial financial support from the Center for Informatics and Computational Science (CICS) at the University of Notre Dame where this work was performed. The work of N.Z. was supported from the Defense Advanced Research Projects Agency under the Physics of Artificial Intelligence program (contract HR00111890034). The computing was supported via an AFOSR-DURIP award with additional resources provided by the University of Notre Dame Center for Research Computing. The work of X.S. and J.W. was supported by the National Natural Science Foundation of China (No. 41730856 and 41672229). The authors would like to thank the three anonymous reviewers and the Editors for their helpful comments. The codes and data used in this work are available at <https://github.com/cics-nd/CAAE-DRDCN-inverse>.

Appendix A Deep dense convolutional network

The deep dense convolutional network (DDCN) for surrogate modeling (Mo, Zabararas, et al., 2019; Mo, Zhu, et al., 2019; Zhu & Zabararas, 2018; Zhu et al., 2019) is based on a dense connection structure called dense block (Huang et al., 2017). The dense block introduces connections between its internal nonadjacent layers to enhance the information propagation through the network, so as to reduce the training sample size required to obtain desired approximation accuracy (Huang et al., 2017). An illustration of the dense block structure is shown in Figure 1a. The difference between the dense blocks used in the DDCN network and in the DRDCN network proposed in this study is that, in DDCN, the input feature

maps of the dense block's last layer are concatenated to its output feature maps to be fed into the next layer; while in DRDCN only the output feature maps of the dense block's last layer are passed to the next layer to allow an element-wise addition operation in the residual learning strategy (see section 3.2.1).

We adopt the DDCN network architecture employed in our previous study (Mo, Zabararas, et al., 2019) which was used for surrogate modeling of a 2-D solute transport model with Gaussian conductivity fields. The ReLU instead of Mish activation was used in DDCN. The network is composed of 27 convolutional layers with three dense blocks. For the 3-D case considered in this study, we directly replace the 2-D convolutional layers in the network with the 3-D convolutional layers. More details about the network architecture can be found in Mo, Zabararas, et al. (2019). When training the DDCN network, we use the same settings as in the DRDCN network. That is, the network is trained using the L_1 loss function defined in equation (19) for 200 epochs in the 2-D case and 300 epochs in the 3-D case with the Adam optimizer (Kingma & Ba, 2014). The batch size is 32 and the initial learning rate is 5×10^{-3} . A learning rate scheduler which drops ten times on plateau during training is used. Python codes of DDCN are available at <https://github.com/cics-nd/cnn-inversion>.

References

- Asher, M. J., Croke, B. F. W., Jakeman, A. J., & Peeters, L. J. M. (2015). A review of surrogate models and their application to groundwater modeling. *Water Resources Research*, *51*(8), 5957-5973. doi: 10.1002/2015WR016967
- Bergen, K. J., Johnson, P. A., de Hoop, M. V., & Beroza, G. C. (2019). Machine learning for data-driven discovery in solid Earth geoscience. *Science*, *363*(6433). doi: 10.1126/science.aau0323
- Canchumuni, S. W., Emerick, A. A., & Pacheco, M. A. C. (2019a). History matching geological facies models based on ensemble smoother and deep generative models. *Journal of Petroleum Science and Engineering*, *177*, 941 - 958. doi: <https://doi.org/10.1016/j.petrol.2019.02.037>
- Canchumuni, S. W., Emerick, A. A., & Pacheco, M. A. C. (2019b). Towards a robust parameterization for conditioning facies models using deep variational autoencoders and ensemble smoother. *Computers & Geosciences*, *128*, 87 - 102. doi: <https://doi.org/10.1016/j.cageo.2019.04.006>
- Chan, S., & Elsheikh, A. H. (2017). Parametrization and generation of geological models with generative adversarial networks. *arXiv e-prints*, arXiv:1708.01810.
- Chan, S., & Elsheikh, A. H. (2018). Parametric generation of conditional geological realizations using generative neural networks. *arXiv e-prints*, arXiv:1807.05207.
- Chan, S., & Elsheikh, A. H. (2019). Parametrization of stochastic inputs using generative adversarial networks with application in geology. *arXiv e-prints*, arXiv:1904.03677.
- Chang, H., Liao, Q., & Zhang, D. (2017). Surrogate model based iterative ensemble smoother for subsurface flow data assimilation. *Advances in Water Resources*, *100*, 96 - 108. doi: <https://doi.org/10.1016/j.advwatres.2016.12.001>
- Cui, T., Fox, C., & O'Sullivan, M. J. (2011). Bayesian calibration of a large-scale geothermal reservoir model by a new adaptive delayed acceptance Metropolis Hastings algorithm. *Water Resources Research*, *47*(10), W10521. doi: 10.1029/2010WR010352
- Elsheikh, A. H., Hoteit, I., & Wheeler, M. F. (2014). Efficient Bayesian inference of subsurface flow models using nested sampling and sparse polynomial chaos surrogates. *Computer Methods in Applied Mechanics and Engineering*, *269*, 515 - 537. doi: <https://doi.org/10.1016/j.cma.2013.11.001>
- Emerick, A. A., & Reynolds, A. C. (2013). Ensemble smoother with multiple data assimilation. *Computers & Geosciences*, *55*, 3 - 15. doi: <https://doi.org/10.1016/j.cageo.2012.03.011>
- Evensen, G. (1994). Sequential data assimilation with a nonlinear quasi-geostrophic model using Monte Carlo methods to forecast error statistics. *Journal of Geophysical Re-*

- search: *Oceans*, 99(C5), 10143-10162. doi: 10.1029/94JC00572
- Gómez-Hernández, J. J., & Wen, X.-H. (1998). To be or not to be multi-Gaussian? A reflection on stochastic hydrogeology. *Advances in Water Resources*, 21(1), 47 - 61. doi: [https://doi.org/10.1016/S0309-1708\(96\)00031-0](https://doi.org/10.1016/S0309-1708(96)00031-0)
- Goodfellow, I., Bengio, Y., & Courville, A. (2016). *Deep learning*. Cambridge, MA, USA: The MIT Press.
- Goodfellow, I., Pouget-Abadie, J., Mirza, M., Xu, B., Warde-Farley, D., Ozair, S., ... Bengio, Y. (2014). Generative adversarial nets. In *Conference on Neural Information Processing Systems (NeurIPS)* (pp. 2672–2680).
- Hansen, T. M., Cordua, K. S., & Mosegaard, K. (2012). Inverse problems with non-trivial priors: Efficient solution through sequential Gibbs sampling. *Computational Geosciences*, 16(3), 593–611. doi: 10.1007/s10596-011-9271-1
- Harbaugh, A. W., Banta, E. R., Hill, M. C., & McDonald, M. G. (2000). *MODFLOW-2000, the U.S. Geological Survey modular ground-water flow model-user guide to modularization concepts and the ground-water flow process* (Tech. Rep. No. Open-File Report 00-92). U.S. Geological Survey.
- He, K., Zhang, X., Ren, S., & Sun, J. (2016a). Deep residual learning for image recognition. In *IEEE Conference on Computer Vision and Pattern Recognition (CVPR)*.
- He, K., Zhang, X., Ren, S., & Sun, J. (2016b). Identity mappings in deep residual networks. In *European Conference on Computer Vision (ECCV)* (pp. 630–645). Springer International Publishing.
- Huang, G., Liu, Z., Maaten, L. V. D., & Weinberger, K. Q. (2017). Densely connected convolutional networks. In *IEEE Conference on Computer Vision and Pattern Recognition (CVPR)* (p. 2261-2269). doi: 10.1109/CVPR.2017.243
- Ioffe, S., & Szegedy, C. (2015). Batch normalization: Accelerating deep network training by reducing internal covariate shift. In *International Conference on Machine Learning (ICML)* (pp. 448–456).
- Journel, A. G., & Deutsch, C. V. (1993). Entropy and spatial disorder. *Mathematical Geology*, 25(3), 329–355. doi: 10.1007/BF00901422
- Ju, L., Zhang, J., Meng, L., Wu, L., & Zeng, L. (2018). An adaptive Gaussian process-based iterative ensemble smoother for data assimilation. *Advances in Water Resources*, 115, 125 - 135. doi: <https://doi.org/10.1016/j.advwatres.2018.03.010>
- Kani, J. N., & Elsheikh, A. H. (2019). Reduced-order modeling of subsurface multi-phase flow models using deep residual recurrent neural networks. *Transport in Porous Media*, 126(3), 713–741. doi: 10.1007/s11242-018-1170-7
- Kerrou, J., Renard, P., Franssen, H.-J. H., & Lunati, I. (2008). Issues in characterizing heterogeneity and connectivity in non-multiGaussian media. *Advances in Water Resources*, 31(1), 147 - 159. doi: <https://doi.org/10.1016/j.advwatres.2007.07.002>
- Kingma, D. P., & Ba, J. (2014). Adam: A method for stochastic optimization. *arXiv e-prints*, arXiv:1412.6980.
- Kingma, D. P., & Welling, M. (2014). Auto-encoding variational Bayes. In *International Conference on Learning Representations (ICLR)*.
- Kitanidis, P. K. (2015). Persistent questions of heterogeneity, uncertainty, and scale in subsurface flow and transport. *Water Resources Research*, 51(8), 5888-5904. doi: 10.1002/2015WR017639
- Krizhevsky, A., Sutskever, I., & Hinton, G. E. (2012). Imagenet classification with deep convolutional neural networks. In F. Pereira, C. J. C. Burges, L. Bottou, & K. Q. Weinberger (Eds.), *Advances in Neural Information Processing Systems* (pp. 1097–1105). Curran Associates, Inc.
- Laloy, E., Héroult, R., Jacques, D., & Linde, N. (2018). Training-image based geostatistical inversion using a spatial generative adversarial neural network. *Water Resources Research*, 54(1), 381-406. doi: 10.1002/2017WR022148
- Laloy, E., Héroult, R., Lee, J., Jacques, D., & Linde, N. (2017). Inversion using a new low-dimensional representation of complex binary geological media based on a deep neural network. *Advances in Water Resources*, 110, 387 - 405. doi: <https://doi.org/>

- 10.1016/j.advwatres.2017.09.029
- Laloy, E., Linde, N., Jacques, D., & Mariethoz, G. (2016). Merging parallel tempering with sequential geostatistical resampling for improved posterior exploration of high-dimensional subsurface categorical fields. *Advances in Water Resources*, *90*, 57 - 69. doi: <https://doi.org/10.1016/j.advwatres.2016.02.008>
- Laloy, E., Linde, N., Ruffino, C., Hrault, R., Gasso, G., & Jacques, D. (2019). Gradient-based deterministic inversion of geophysical data with generative adversarial networks: Is it feasible? *Computers & Geosciences*, *133*, 104333. doi: <https://doi.org/10.1016/j.cageo.2019.104333>
- Laloy, E., Rogiers, B., Vrugt, J. A., Mallants, D., & Jacques, D. (2013). Efficient posterior exploration of a high-dimensional groundwater model from two-stage Markov chain Monte Carlo simulation and polynomial chaos expansion. *Water Resources Research*, *49*(5), 2664-2682. doi: [10.1002/wrcr.20226](https://doi.org/10.1002/wrcr.20226)
- Ledig, C., Theis, L., Huszar, F., Caballero, J., Cunningham, A., Acosta, A., ... Shi, W. (2017). Photo-realistic single image super-resolution using a generative adversarial network. In *IEEE Conference on Computer Vision and Pattern Recognition (CVPR)*.
- Liao, Q., Zhang, D., & Tchelepi, H. (2017). A two-stage adaptive stochastic collocation method on nested sparse grids for multiphase flow in randomly heterogeneous porous media. *Journal of Computational Physics*, *330*, 828 - 845. doi: <https://doi.org/10.1016/j.jcp.2016.10.061>
- Lin, G., & Tartakovsky, A. (2009). An efficient, high-order probabilistic collocation method on sparse grids for three-dimensional flow and solute transport in randomly heterogeneous porous media. *Advances in Water Resources*, *32*(5), 712 - 722. doi: <https://doi.org/10.1016/j.advwatres.2008.09.003>
- Linde, N., Renard, P., Mukerji, T., & Caers, J. (2015). Geological realism in hydrogeological and geophysical inverse modeling: A review. *Advances in Water Resources*, *86*, 86-101. doi: <https://doi.org/10.1016/j.advwatres.2015.09.019>
- Lipowski, A., & Lipowska, D. (2012). Roulette-wheel selection via stochastic acceptance. *Physica A: Statistical Mechanics and its Applications*, *391*(6), 2193 - 2196. doi: <https://doi.org/10.1016/j.physa.2011.12.004>
- Liu, Q., & Wang, D. (2016). Stein variational gradient descent: A general purpose Bayesian inference algorithm. In D. D. Lee, M. Sugiyama, U. V. Luxburg, I. Guyon, & R. Garnett (Eds.), *Advances in Neural Information Processing Systems* (pp. 2378-2386). Curran Associates, Inc.
- Liu, Y., Sun, W., & Durlofsky, L. J. (2019). A deep-learning-based geological parameterization for history matching complex models. *Mathematical Geosciences*. doi: [10.1007/s11004-019-09794-9](https://doi.org/10.1007/s11004-019-09794-9)
- Ma, X., & Zabaras, N. (2011). Kernel principal component analysis for stochastic input model generation. *Journal of Computational Physics*, *230*(19), 7311 - 7331. doi: <https://doi.org/10.1016/j.jcp.2011.05.037>
- Makhzani, A., Shlens, J., Jaitly, N., & Goodfellow, I. (2016). Adversarial autoencoders. In *International Conference on Learning Representations (ICLR)*.
- Mariethoz, G., Renard, P., & Caers, J. (2010). Bayesian inverse problem and optimization with iterative spatial resampling. *Water Resources Research*, *46*(11), W11530. doi: [10.1029/2010WR009274](https://doi.org/10.1029/2010WR009274)
- Misra, D. (2019). Mish: A self regularized non-monotonic neural activation function. *arXiv e-prints*, arXiv:1908.08681.
- Mo, S., Lu, D., Shi, X., Zhang, G., Ye, M., Wu, J., & Wu, J. (2017). A Taylor expansion-based adaptive design strategy for global surrogate modeling with applications in groundwater modeling. *Water Resources Research*, *53*(12), 10802-10823. doi: [10.1002/2017WR021622](https://doi.org/10.1002/2017WR021622)
- Mo, S., Zabaras, N., Shi, X., & Wu, J. (2019). Deep autoregressive neural networks for high-dimensional inverse problems in groundwater contaminant source identification. *Water Resources Research*, *55*(5), 3856-3881. doi: [10.1029/2018WR024638](https://doi.org/10.1029/2018WR024638)
- Mo, S., Zhu, Y., Zabaras, N., Shi, X., & Wu, J. (2019). Deep convolutional encoder-decoder

- networks for uncertainty quantification of dynamic multiphase flow in heterogeneous media. *Water Resources Research*, *55*(1), 703–728. doi: 10.1029/2018WR023528
- Oliver, D. S., & Chen, Y. (2011). Recent progress on reservoir history matching: A review. *Computational Geosciences*, *15*(1), 185–221. doi: 10.1007/s10596-010-9194-2
- Rasmussen, C. E., & Williams, C. K. (2006). *Gaussian processes for machine learning*. Cambridge, MA, USA: MIT Press.
- Razavi, S., Tolson, B. A., & Burn, D. H. (2012). Review of surrogate modeling in water resources. *Water Resources Research*, *48*(7), W07401. doi: 10.1029/2011WR011527
- Reichstein, M., Camps-Valls, G., Stevens, B., Jung, M., Denzler, J., Carvalhais, N., & Prabhat. (2019). Deep learning and process understanding for data-driven Earth system science. *Nature*, *566*(7743). doi: 10.1038/s41586-019-0912-1
- Sarma, P., Durlofsky, L. J., & Aziz, K. (2008). Kernel principal component analysis for efficient, differentiable parameterization of multipoint geostatistics. *Mathematical Geosciences*, *40*(1), 3–32. doi: 10.1007/s11004-007-9131-7
- Shen, C. (2018). A transdisciplinary review of deep learning research and its relevance for water resources scientists. *Water Resources Research*, *54*(11), 8558–8593. doi: 10.1029/2018WR022643
- Simonyan, K., & Zisserman, A. (2015). Very deep convolutional networks for large-scale image recognition. In *International Conference on Learning Representations (ICLR)*.
- Strebelle, S. (2002). Conditional simulation of complex geological structures using multiple-point statistics. *Mathematical Geology*, *34*(1), 1–21. doi: 10.1023/A:1014009426274
- Sun, A. Y. (2018). Discovering state-parameter mappings in subsurface models using generative adversarial networks. *Geophysical Research Letters*, *45*(20), 11,137–11,146. doi: 10.1029/2018GL080404
- Sun, A. Y., Morris, A. P., & Mohanty, S. (2009). Sequential updating of multimodal hydrogeologic parameter fields using localization and clustering techniques. *Water Resources Research*, *45*(7), W07424. doi: 10.1029/2008WR007443
- Szegedy, C., Ioffe, S., & Vanhoucke, V. (2016). Inception-v4, inception-resnet and the impact of residual connections on learning. *arXiv e-prints*, arXiv:1602.07261.
- Szegedy, C., Liu, W., Jia, Y., Sermanet, P., Reed, S., Anguelov, D., . . . Rabinovich, A. (2015). Going deeper with convolutions. In *IEEE Conference on Computer Vision and Pattern Recognition (CVPR)*.
- Tripathy, R. K., & Bilonis, I. (2018). Deep UQ: Learning deep neural network surrogate models for high dimensional uncertainty quantification. *Journal of Computational Physics*, *375*, 565 - 588. doi: <https://doi.org/10.1016/j.jcp.2018.08.036>
- van Leeuwen, P. J., & Evensen, G. (1996). Data assimilation and inverse methods in terms of a probabilistic formulation. *Monthly Weather Review*, *124*(12), 2898–2913. doi: 10.1175/1520-0493(1996)124<2898:DAAIMI>2.0.CO;2
- Vo, H. X., & Durlofsky, L. J. (2014). A new differentiable parameterization based on principal component analysis for the low-dimensional representation of complex geological models. *Mathematical Geosciences*, *46*(7), 775–813. doi: 10.1007/s11004-014-9541-2
- Vrugt, J. A. (2016). Markov chain Monte Carlo simulation using the DREAM software package: Theory, concepts, and MATLAB implementation. *Environmental Modelling & Software*, *75*, 273 - 316. doi: <https://doi.org/10.1016/j.envsoft.2015.08.013>
- Wang, X., Yu, K., Wu, S., Gu, J., Liu, Y., Dong, C., . . . Change Loy, C. (2018). ESRGAN: Enhanced super-resolution generative adversarial networks. In *European Conference on Computer Vision (ECCV)*.
- Wang, Z., Bovik, A. C., Sheikh, H. R., & Simoncelli, E. P. (2004). Image quality assessment: From error visibility to structural similarity. *IEEE Transactions on Image Processing*, *13*(4), 600–612. doi: 10.1109/TIP.2003.819861
- Winter, C., Tartakovsky, D., & Guadagnini, A. (2003). Moment differential equations for flow in highly heterogeneous porous media. *Surveys in Geophysics*, *24*(1), 81–106. doi: 10.1023/A:1022277418570
- Xiu, D., & Karniadakis, G. (2002). The Wiener–Askey polynomial chaos for stochastic differential equations. *SIAM Journal on Scientific Computing*, *24*(2), 619–644. doi:

10.1137/S1064827501387826

- Xu, T., & Gómez-Hernández, J. J. (2018). Simultaneous identification of a contaminant source and hydraulic conductivity via the restart normal-score ensemble Kalman filter. *Advances in Water Resources*, *112*, 106 - 123. doi: <https://doi.org/10.1016/j.advwatres.2017.12.011>
- Zahner, T., Lochbühler, T., Mariethoz, G., & Linde, N. (2016). Image synthesis with graph cuts: A fast model proposal mechanism in probabilistic inversion. *Geophysical Journal International*, *204*(2), 1179-1190. doi: 10.1093/gji/ggv517
- Zhang, D., & Lu, Z. (2004). An efficient, high-order perturbation approach for flow in random porous media via Karhunen-Loève and polynomial expansions. *Journal of Computational Physics*, *194*(2), 773 - 794. doi: <https://doi.org/10.1016/j.jcp.2003.09.015>
- Zhang, J., Li, W., Zeng, L., & Wu, L. (2016). An adaptive Gaussian process-based method for efficient Bayesian experimental design in groundwater contaminant source identification problems. *Water Resources Research*, *52*(8), 5971-5984. doi: 10.1002/2016WR018598
- Zhang, J., Lin, G., Li, W., Wu, L., & Zeng, L. (2018). An iterative local updating ensemble smoother for estimation and uncertainty assessment of hydrologic model parameters with multimodal distributions. *Water Resources Research*, *54*(3), 1716-1733. doi: 10.1002/2017WR020906
- Zhang, J., Zeng, L., Chen, C., Chen, D., & Wu, L. (2015). Efficient Bayesian experimental design for contaminant source identification. *Water Resources Research*, *51*(1), 576-598. doi: 10.1002/2014WR015740
- Zheng, C., & Wang, P. P. (1999). MT3DMS: A modular three-dimensional multi-species transport model for simulation of advection, dispersion, and chemical reactions of contaminants in ground-water systems. documentation and user's guide. In *Contract Report SERDP-99-1, Environmental Laboratory, U.S. Army Engineering Research and Development*.
- Zhong, Z., Sun, A. Y., & Jeong, H. (2019). Predicting CO₂ plume migration in heterogeneous formations using conditional deep convolutional generative adversarial network. *Water Resources Research*, *55*. doi: 10.1029/2018WR024592
- Zhou, H., Gómez-Hernández, J. J., Franssen, H.-J. H., & Li, L. (2011). An approach to handling non-Gaussianity of parameters and state variables in ensemble Kalman filtering. *Advances in Water Resources*, *34*(7), 844 - 864. doi: <https://doi.org/10.1016/j.advwatres.2011.04.014>
- Zhou, H., Gómez-Hernández, J. J., & Li, L. (2014). Inverse methods in hydrogeology: Evolution and recent trends. *Advances in Water Resources*, *63*, 22 - 37. doi: <https://doi.org/10.1016/j.advwatres.2013.10.014>
- Zhu, Y., & Zabaras, N. (2018). Bayesian deep convolutional encoder-decoder networks for surrogate modeling and uncertainty quantification. *Journal of Computational Physics*, *366*, 415 - 447. doi: <https://doi.org/10.1016/j.jcp.2018.04.018>
- Zhu, Y., Zabaras, N., Koutsourelakis, P.-S., & Perdikaris, P. (2019). Physics-constrained deep learning for high-dimensional surrogate modeling and uncertainty quantification without labeled data. *Journal of Computational Physics*, *394*, 56 - 81. doi: <https://doi.org/10.1016/j.jcp.2019.05.024>
- Zuo, R., Xiong, Y., Wang, J., & Carranza, E. J. M. (2019). Deep learning and its application in geochemical mapping. *Earth-Science Reviews*, *192*, 1-14. doi: <https://doi.org/10.1016/j.earscirev.2019.02.023>